Precambrian Research 266 (2015) 86–107

Contents lists available at ScienceDirect

Precambrian Research

journal homepage: www.elsevier.com/locate/precamres

Geochronology, mineralogy and geochemistry of alkali-feldspar granite and albite granite association from the Changyi area of Jiao-Liao-Ji Belt: Implications for Paleoproterozoic rifting of eastern North China Craton

Ting-Guang Lan[a,b,*], Hong-Rui Fan[b], Kui-Feng Yang[b], Ya-Chun Cai[b], Bo-Jie Wen[b], Wen Zhang[c]

[a] State Key Laboratory of Ore Deposit Geochemistry, Institute of Geochemistry, Chinese Academy of Sciences, Guiyang 550081, China
[b] Key Laboratory of Mineral Resources, Institute of Geology and Geophysics, Chinese Academy of Sciences, Beijing 100029, China
[c] Tianjin North China Geological Exploration General Institute, Tianjin 300170, China

ARTICLE INFO

Article history:
Received 19 October 2014
Received in revised form 17 April 2015
Accepted 29 April 2015
Available online 11 May 2015

Keywords:
A-type granite
Albite granite
Paleoproterozoic
Continental rift
Jiao-Liao-Ji Belt
North China Craton

ABSTRACT

Paleoproterozoic granites, divided into alkali-feldspar granite and albite granite, were newly discovered in the Changyi area of the Jiao-Liao-Ji Belt from the Eastern Block of the North China Craton. LA–ICP-MS zircon U–Pb dating shows that the alkali-feldspar granite was emplaced at 2193 Ma, whereas the albite granite intruded at 2171 Ma. These granites have high SiO_2, $Na_2O + K_2O$, Zr, Nb, Ga, Y and HREE contents and show remarkably low CaO, Eu, Ba and Sr concentrations, strongly suggesting their A-type affinities. Zircon saturation thermometry and Al^T-in-biotite geobarometer indicate that the alkali-feldspar granite crystallized at temperatures of 823–856 °C (averaging at 839 °C) and pressures of 1.54–2.73 kbar (averaging at 2.05 kbar) while the albite granite was cooled at the temperatures of 851–853 °C and the pressures of 2.34–2.64 kbar (averaging at 2.45 kbar). Combined with such high temperatures and low pressures, the crustal-like Nd–Hf isotopic compositions ($\varepsilon_{Nd}(t) = -5.3$ to -4.4, $\varepsilon_{Hf}(t) = -7.0$ to -3.8.) support their derivation from the shallow melting of Archean crustal rocks under high heat flow. However, the contrasted K_2O and Na_2O compositions between the alkali-feldspar granite ($K_2O = 4.76$–5.14 wt.%, $Na_2O = 4.76$–5.14 wt.%) and the albite granite ($K_2O = 0.29$–0.44 wt.%, $Na_2O = 6.15$–6.56 wt.%) imply that they may have been derived from distinct source rocks or have undergone different magmatic processes. Genetic modeling suggests that the alkali-feldspar granite was originated from melting of granodioritic rocks. The albite granite, however, was most likely derived from the reworking of plagioclase-rich layers after the extraction of A-type melts. Coupled with other studies on sedimentary and volcanic successions in the Jiao-Liao-Ji Belt, the unusual association of the A-type alkali-feldspar granite and albite granite indicates that the southern segment of the Jiao-Liao-Ji Belt experienced continental rifting during 2.1–2.2 Ga.

1. Introduction

The North China Craton (NCC), one of the oldest cratons in the world (Liu et al., 1992) and the largest one in China (Zhai and Santosh, 2011), has attracted considerable attentions in recent years due to the complicated amalgamation during early Precambrian time (e.g., Kusky, 2011; Santosh, 2010; Zhai and Santosh, 2011; Zhao et al., 2012; Zhao and Zhai, 2013) and the typical craton destruction during Phanerozoic time (e.g., Gao et al., 2009; Xu et al., 2009, Xu et al., 2013; Zhang et al., 2013; Zhu et al., 2012). Former studies have contributed a lot to reveal the tectonic processes of the craton, which show that the NCC was built by amalgamation of a number of Archean micro-continental blocks (e.g., Kusky, 2011; Zhai and Santosh, 2011; Zhao and Cawood, 2012; Zhao et al., 2012). However, the number of constituent blocks, and when and how they were assembled to form the coherent basement of the craton remain unresolved (Zhao et al., 2012). Two representative models have been hotly debated, with one considering that amalgamation among seven Archean micro-blocks constructed the NCC

* Corresponding author at: 99 Linchengxilu Road, Guanshanhu District, Guiyang City, Guizhou Province, China. Tel.: +86 851 84828426.
E-mail address: lantingguang@126.com (T.-G. Lan).

http://dx.doi.org/10.1016/j.precamres.2015.04.021
0301-9268/

at the end of Archean (ca. 2.5 Ga) and subsequently the NCC experienced an orogenic cycle from rifting to subduction–collision along three belts during Paleoproterozoic time (2350–1970 Ma) (Zhai and Santosh, 2011, and references therein), whereas the other regards that four Archean micro-continental blocks constructed the NCC through continuous subduction–collision during Paleoproterozoic time (from 1.95 to 1.85 Ga) (Zhao, 2001; Zhao et al., 2005, 2012). Other models favoring multi-stage subduction–collision and/or rifting during Archean and Paleoproterozoic were also proposed (e.g., Faure et al., 2007; Kusky, 2011). One of approaches to resolve these controversies is to determine whether these discrete continental blocks were separated from each other by vast oceans or by intra-continental rifts during Paleoproterozoic time. Therefore, identifying the Paleoproterozoic tectonic setting becomes vital in understanding the history of the NCC.

As one of the three famous Paleoproterozoic belts in the NCC, the Jiao-Liao-Ji Belt is located at the Eastern Block of the NCC (Fig. 1). It has long been debated that whether the belt experienced opening and closing of a continental rift (e.g., Li et al., 2005, 2006, 2011a; Li and Zhao, 2007; Luo et al., 2004, 2008; Peng and Palmer, 1995; Yu, 1996; Zhao et al., 2005) or suffered amalgamation processes between independent continental terranes (e.g., Faure et al., 2004; He and Ye, 1998; Li and Chen, 2014; Lu et al., 2006; Meng et al., 2013, 2014). Bimodal volcanic rocks (Peng and Palmer, 1995; Sun et al., 1996; Yu, 1996; Zhang and Yang, 1988), A-type granites (Chen et al., 2001; Hao et al., 2004; Li and Yang, 1997; Li and Zhao, 2007), anticlockwise *P–T* paths (Dong and Wang, 1998; Li et al., 2001; Lu, 1996) and non-marine borate-bearing sedimentary successions (Hu et al., 2015; Jiang et al., 1997; Peng and Palmer, 1995, 2002) were considered as the robust evidence for a Paleoproterozoic continental rift. However, sediments (e.g., Meng et al., 2013) and meta-mafic rocks (e.g., Li and Chen, 2014; Meng et al., 2014) with active continental margin signatures and clockwise *P–T* paths (e.g., He and Ye, 1998; Tam et al., 2012a,b,c; Wang et al., 2010; Zhou et al., 2007) were also observed in the belt, which support the subduction–collision processes between independent continental terranes. Recently, Paleoproterozoic A-type granites were discovered in the Changyi area of western Jiaobei massif located at the middle section of the Jiao-Liao-Ji Belt (Fig. 1b). As the A-type granites can provide significant information on post-collisional/intra-plate extensional magmatic processes within continental lithosphere (e.g., Eby, 1990, 1992), we carried out detailed and comprehensive geochronological, mineralogical, geochemical and isotopic investigations on the Changyi A-type granites, with an aim to constrain the Paleoproterozoic tectonic setting of the eastern NCC.

2. Geological setting

Three major Paleoproterozoic belts have been recognized in the NCC (Fig. 1a), commonly termed the Khondalite Belt in the northwest, the Trans-North China Orogen in the middle and the Jiao-Liao-Ji Belt in the east (Zhao et al., 2001, 2005, 2012). The metasedimentary rocks in these three belts contain the youngest detrital zircons of 2.0–2.33 Ga and show the regional metamorphic ages of 1.85–1.88 Ga, which limit the depositional time of the sediments to be 1.88–2.0 Ga (Wan et al., 2006). In the Jiao-Liao-Ji Belt, the Paleoproterozoic successions consist of the Macheonayeong Group in North Korea, the Laoling and Ji'an groups in the southern Jilin Province, the North and South Liaohe groups in the eastern Liaoning Peninsula, the Fenzishan and Jingshan groups in the Jiaobei Massif, and the Wuhe Group in the Anhui Province (Fig. 1b), which are transitional from a basal clastic-rich sequence and a lower bimodal-volcanic sequence, through a middle carbonate-rich sequence, to an upper pelite-rich sequence (Zhao et al., 2012, and references therein). Based on the comparable features among the stratigraphical groups, the belt is generally divided into a northern zone, which comprises the Laoling, North Liaohe and Fenzishan groups, and a southern zone that consists of the Ji'an, South Liaohe and Jingshan groups (Fig. 1b, Zhao et al., 2005). The northern and southern zones may have undergone different metamorphic processes, since clockwise and anticlockwise metamorphic *P–T* paths were respectively recognized in the northern and southern zones (e.g., He and Ye, 1998; Li et al., 2001, 2011a; Lu, 1996). Recently, clockwise metamorphic *P–T* path was also identified in the Jingshan Group from the southern zone (e.g., Li et al., 2011b; Tam et al., 2012a,b,c; Wang et al., 2010; Zhou et al., 2007), which may lead to the re-interpretation of the evolution of the Jiao-Liao-Ji Belt.

Paleoproterozoic granitoids and minor mafic intrusions also occurred in the belt, of which the granitoid plutons are mainly deformed A-type granites and undeformed alkaline syenites and rapakivi granites (e.g., Hao et al., 2004; Li et al., 2005; Li and Yang, 1997; Li and Zhao, 2007; Liu et al., 2014; Lu et al., 2004, 2005, 2006; Yang et al., 2009; Zhang and Yang, 1988; Zhao et al., 2012), and the mafic intrusions consist of gabbros and dolerites metamorphosed from greenschist facies to amphibolite facies (Li et al., 2005; Lu et al., 2006; Meng et al., 2014). The deformed A-type granites were emplaced at 2.1–2.2 Ga, whereas the undeformed alkaline syenites and rapakivi granites were dated at 1.8–1.9 Ga (e.g., Hao et al., 2004; Liu et al., 2014; Lu et al., 2004, 2005; Li and Zhao, 2007). The granitoid intrusions have been mainly found in the southern Jilin Province, eastern Liaoning Peninsula and Bengbu area of Anhui Province, but rarely outcrop in the Jiaobei massif. In recent years, some Paleoproterozoic granites are discovered in the Changyi area of Jiaobei massif due to the deep mining of iron ores (from the Changyi iron deposit, Lan et al., 2014a,b). The newly discovered granites intruded into the Paleoproterozoic Fenzishan Group at the depth >−190 m (Fig. 2) and strongly altered and deformed the metamorphic wallrocks (Fig. 3a and b), suggesting that the emplacement of the granites occurred at some time later than the deposition of the Fengzishan Group. This finding is inconsistent with the previous reports of the Paleoproterozoic A-type Liaoji granites (~2160 Ma) in the Tonghua area of southern Jilin Province which considered that the Liaoji granites were emplaced before the deposition of the Paleoproterozoic sequences (e.g., Li and Zhao, 2007; Lu et al., 2004, 2006).

3. Sample description

Two types of granites are observed in the Changyi area (from the Changyi iron deposit). The first type, termed alkali-feldspar granite (Fig. 3c), widely spreads in the mining sections changing from −190 m to −270 m and shows gneissic structure. It consists mainly of feldspar and quartz with subordinate biotite and accessory zircon and apatite (Fig. 3e). The volumetrically dominant (~60 vol.%) feldspar crystals are subhedral to anhedral with grain size varying largely from 0.2 to 2.7 mm, most of which concentrate at the size of 0.5–1 mm. They occur either as interstitial grains or as megacrysts. Both K-feldspar and albite are recognized and they are commonly shown as perthites or intergrown with each other (Fig. 3e and f). Quartz grains (<40 vol.%) are anhedral and interstitial with size of 0.1–2 mm. The scattered biotite crystals (1–2 vol.%) are also anhedral and partially chloritized (Fig. 3e).

The second type, classified as albite granite (Fig. 3d), shows much smaller scale than the first type and is only found at the mining section of −190 m. This granite shows gneissic structure locally and consists mainly of albite and quartz with subordinate biotite and accessory zircon (Fig. 3g and h). The albite crystals (~55 vol.%) are subhedral to anhedral with coarse size of 0.4–3 mm. They occur as interstitial grains or as megacrysts. Fine-grained quartz and euhedral zircon inclusions are commonly observed in the coarse

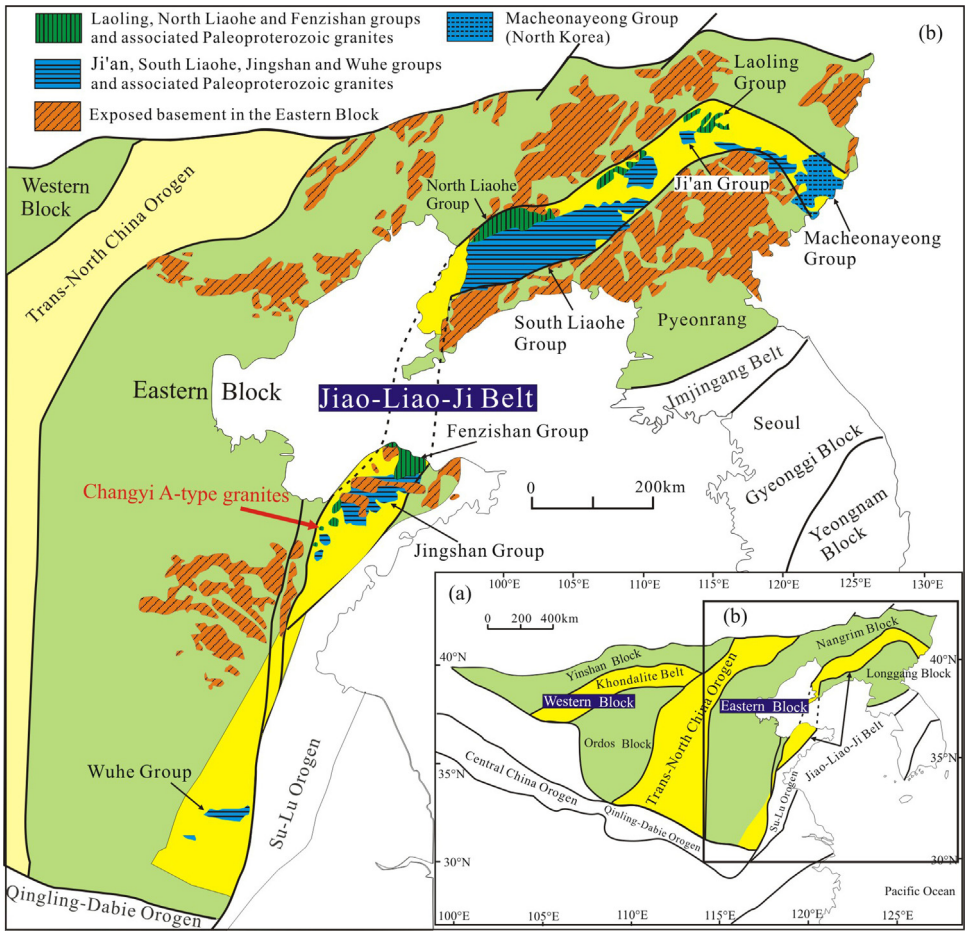

Fig. 1. Tectonic subdivision of the North China Craton (a) and the sketch map of the Paleoproterozoic Jiao-Liao-Ji Belt in the Eastern Block of the NCC (b). Both (a) and (b) are modified after Zhao et al. (2005). Generally, the maps tell that the Yinshan Block collided with the Ordos Block to form the Western Block along the Khondalite Belt at ca. 1.95 Ga and the Longgang Block collided with the Nangrim Block to form the Eastern Block along the Jiao-Liao-Ji Belt at ca. 1.90 Ga. The final cratonization of the NCC was accomplished by the collision between the Eastern and Western blocks along the Trans-North China Orogen at ca. 1.85 Ga (Zhao et al., 2005, 2012). The location of the Changyi A-type granites is also shown in (b).

albite grains (Fig. 3h). The granular quartz crystals (~45 vol.%) are anhedral and interstitial with size changing from 0.1 to 2 mm. Both the albite and quartz grains are poikilitic. Biotite crystals (<1 vol.%) are sporadically found with small size of <1 mm. The sampling of the albite granite becomes difficult due to the rare outcrops.

4. Analytical methods

4.1. Electron microprobe analyses

Electron microprobe analyses were performed with a JEOL JXA-8100 microprobe at the Beijing Research Institute of Uranium Geology. The operating conditions were 20 kV accelerating voltage and 10 nA beam current. Calibration was carried out using the standards provided by SPI Company. Matrix effects were corrected using the ZAF software provided by the JEOL.

4.2. Major and trace elements

Eleven representative samples were selected for major and trace elements analyses at the Institute of Geology and Geophysics, Chinese Academy of Sciences (IGGCAS). For major elements analyses, 200 mesh whole-rock powders (0.5 g) admixed with $Li_2B_4O_7 + LiBO_2$ (5 g) were made into glass discs firstly and then analyzed by X-ray fluorescence spectroscopy (XRF) with an AXIOS Minerals spectrometer. The analytical uncertainties were within 0.1–1% (RSD). For trace element analyses, whole-rock powders (40 mg) were dissolved in distilled $HF + HNO_3$ mixture in Teflon screw-cap capsules at 200 °C for 5 days, dried, and then digested with HNO_3 at 150 °C for 1 day. The final step was repeated once. Dissolved samples were diluted to 49 ml with 1% HNO_3 and 1 ml 500 ppb indium was added to the solution as an internal standard. Trace element abundances were determined by inductively coupled plasma mass spectrometry (ICP-MS) using an ELEMENT spectrometer, which has analytical uncertainties within 5% for most elements.

4.3. Sr–Nd isotopes

Eight fresh samples were selected for Sr–Nd isotopic analyses. Whole-rock powders (200 mesh) for Sr and Nd isotopic analyses were dissolved in Teflon screw-cap capsules after being spiked with ^{87}Rb, ^{84}Sr, ^{149}Sm and ^{150}Nd tracers prior to $HF + HNO_3 + HClO_4$ dissolution. Rb, Sr, Sm and Nd were separated using conventional ion exchange procedures and measured using a Finnigan MAT262 multi-collector mass spectrometer at the IGGCAS. Procedural blanks are <100 pg for Sm and Nd and <300 pg for Rb and Sr. The isotopic ratios were corrected for mass fractionation by normalizing to $^{86}Sr/^{88}Sr = 0.1194$ and $^{146}Nd/^{144}Nd = 0.7219$, respectively. The measured values for the JNdi-1 Nd standard and NBS987 Sr standard were $^{143}Nd/^{144}Nd = 0.512108 \pm 11$ (2σ, $n = 5$) and $^{87}Sr/^{86}Sr = 0.710256 \pm 11$ (2σ, $n = 5$), respectively. USGS

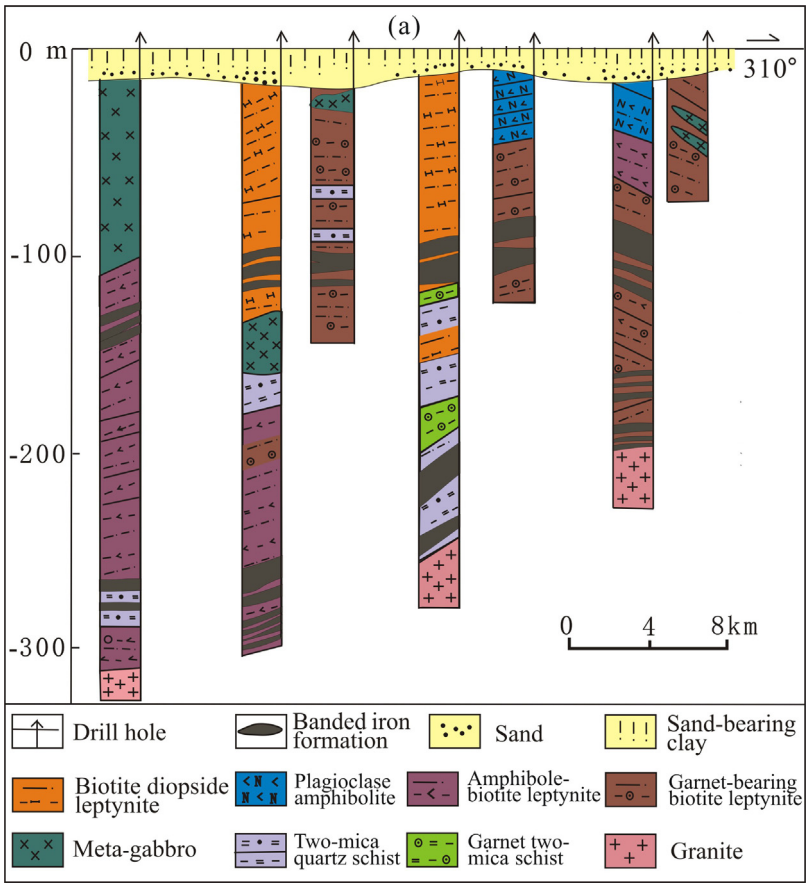

Fig. 2. Profile map of drill holes along exploration line 102 from the Changyi iron deposit showing the intrusion of the Paleoproterozoic granites into the Fenzishan Group (modified after Wang et al., 2007).

reference material BCR-2 was measured to monitor the accuracy of the analytical procedures, with the following results: $^{143}Nd/^{144}Nd = 0.512633 \pm 13$ (2σ) and $^{87}Sr/^{86}Sr = 0.705035 \pm 12$ (2σ). The $^{87}Sr/^{86}Sr$ and $^{143}Nd/^{144}Nd$ data of the BCR-2 show good agreement with previously published data by TIMS and MC–ICP-MS techniques (Li et al., 2012a,b). Detailed analytical procedures were similar to those described by Li et al. (2012a).

4.4. Zircon in situ U–Pb dating and Hf isotopic analyses

Cathodoluminescence (CL) images were obtained using a LEO1450VP scanning electron microscope at the IGGCAS, in order to identify zircon internal textures and choose potential target sites for U–Pb dating and Hf isotopic analyses. The working conditions were at 15 kV.

U–Pb dating and trace element analyses of zircon were conducted synchronously by LA–ICP-MS at the State Key Laboratory of Geological Processes and Mineral Resources, China University of Geosciences, Wuhan. Detailed operating conditions for the laser ablation system, the ICP-MS instrument, and the data reduction process are described by Liu et al. (2008, 2010). Laser sampling was performed using a GeoLas 2005. An Agilent 7500a ICP-MS instrument was used to acquire ion-signal intensities. Each analysis incorporated a background acquisition of approximately 20–30 s (gas blank) followed by 50 s data acquisition from the sample. The Agilent Chemstation was utilized for the acquisition of each individual analysis. Off-line selection and integration of background and analyte signals, time-drift correction, and quantitative calibration for trace element analyses and U–Pb dating were performed by *ICPMSDataCal* (Liu et al., 2008, 2010). Zircon 91500 was used as external standard for U–Pb dating, and was analyzed twice every 5 analyses. Laser spot size of 32 μm and laser repetition of 6 Hz were used during the analyses. Concordia diagrams and weighted mean calculations were made using Isoplot/Ex ver3 (Ludwig, 2003).

Hf isotopic compositions were determined by a Neptune MC-ICP-MS equipped with a GeoLasPlus 193 nm ArF excimer laser at the IGGCAS. Laser spot size of 50 μm and laser repetition of 6 Hz were used during the analyses. The signal collection model is one block with 200 cycles. Each cycle has 0.131 s integration time and total time is about 26 s during each analyses. Zircon Mud Tank was used as external standard for Hf isotopic analyses and was analyzed twice every 5 analyses. Repeated analyses of the Mud Tank yielded a mean $^{176}Hf/^{177}Hf$ ratio of 0.282508 ± 33 (2σ, $n = 49$), which is well consistent with the recommended values within 2σ error (Griffin et al., 2006; Woodhead and Hergt, 2005; Yuan et al., 2008). Detailed analytical procedures were described by Xie et al. (2008).

5. Results

5.1. Geochronology

5.1.1. Alkali-feldspar granite

Zircon crystals in the alkali-feldspar granite (sample CY2-92) range from 80 to 200 μm in size, with length to width ratios of 1:1–3:1. Most of them vary between 100 μm and 150 μm and show subhedral to anhedral shapes. The zircons are gray to dark with moderate oscillatory zoning in CL images (Fig. 4a), which probably imply high U, REE and Th contents in the zircons (Wu and Zheng,

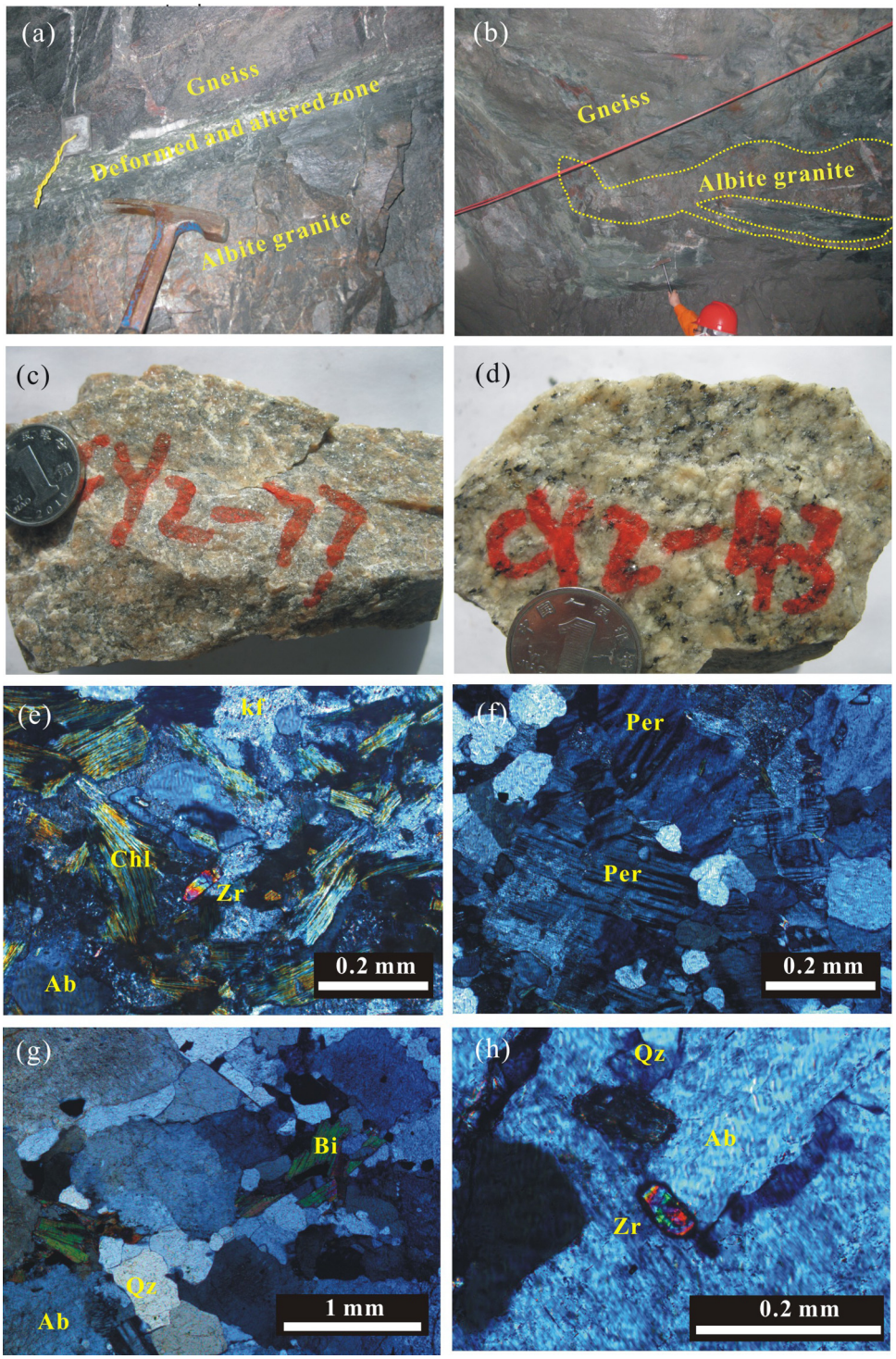

Fig. 3. Representative photographs of the granites intruding into the metamorphic wallrocks (a and b), the hand-specimens of the alkali-feldspar granite (c) and the albite granite (d) and the micrographs of the alkali-feldspar granite (e and f) and the albite granite (g and h). *Note*: biotites in the alkali-feldspar are partially chloritized (e), perthites are common in the alkali-feldspar granite (f), and euhedral zircon grain is enclosed in the albite grain (h). Qz, quartz; Kf, K-feldspar; Ab, albite; Per, perthite; Bi, biotite; Chl, chlorite; Zr, zircon.

2004). In addition, the zircons commonly show alteration features in the rims (Fig. 4a), indicating certain deuteric modification. Nonetheless, twenty-two analyses obtained from well-crystallized or none-altered grains are plotted on or near the concordant line, which yield a mean $^{207}Pb/^{206}Pb$ age of 2193 ± 11 Ma (2σ) (Fig. 5a and Table 1). This age is interpreted as the intrusive age of the alkali-feldspar granite.

5.1.2. Albite granite

Zircon grains in the albite granite (sample CY2-43) range from 100 to 200 μm in size, with length to width ratios of 1:1–2.5:1. Most of the zircon crystals are euhedral to subhedral with moderate oscillatory zoning. They are commonly darker than those of the alkali-feldspar granite in CL images (Fig. 4b). Many cracks occur in the zircons, leading to the difficulties in obtaining concordant ages.

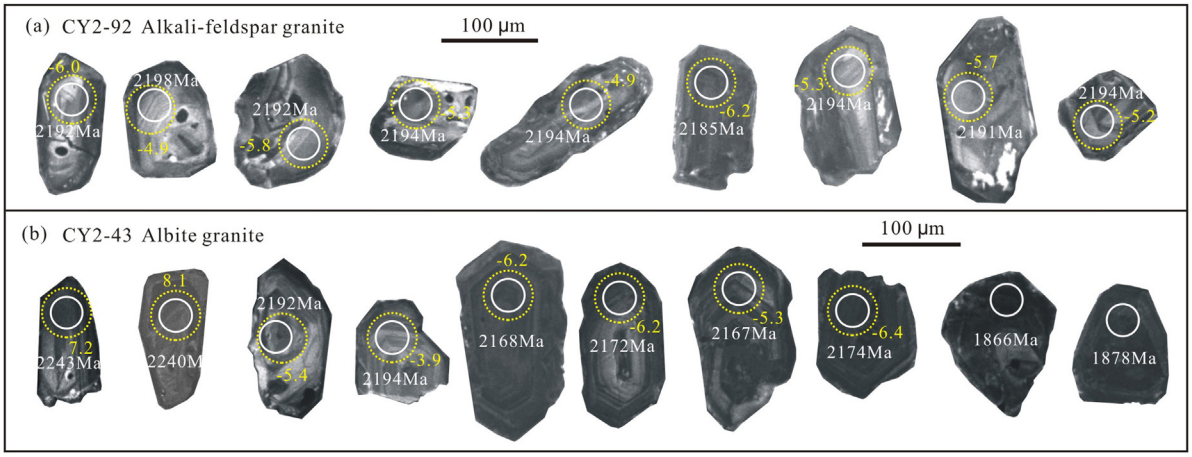

Fig. 4. Representative CL images of zircon grains from the alkali-feldspar granite (a) and the albite granite (b). Zircon $^{207}Pb/^{206}Pb$ ages (Ma) and $\varepsilon_{Hf}(t)$ values are also shown. The bigger circles (dotted line) represent locations of Hf isotopic analyses, whereas the smaller circles indicate spots of LA–ICP-MS U–Pb dating.

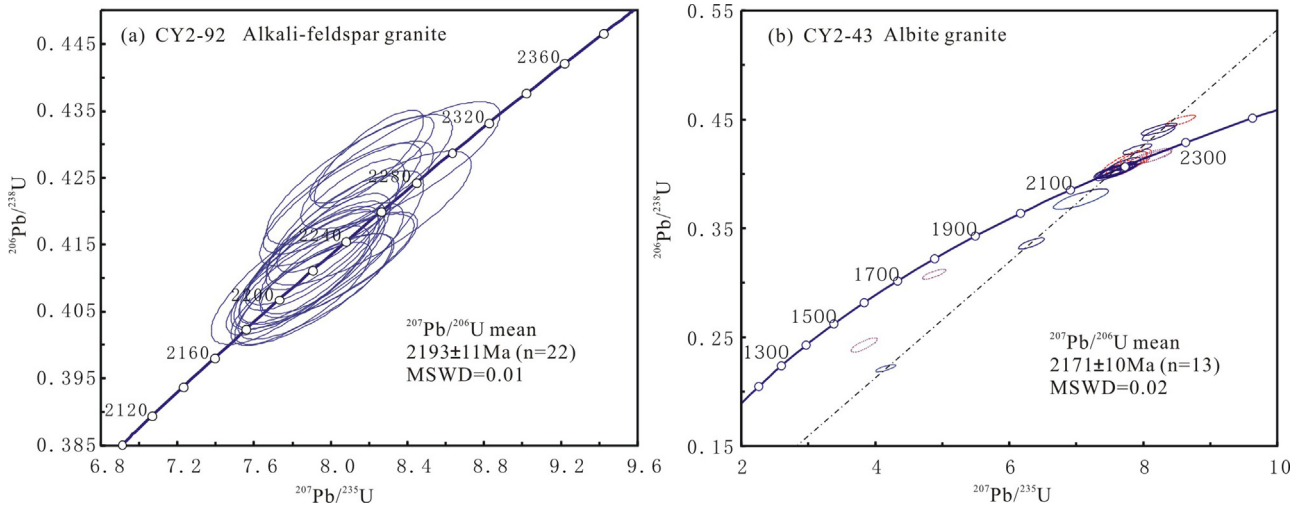

Fig. 5. LA–ICP-MS zircon U–Pb concordia diagrams of the alkali-feldspar granite (a) and the albite granite (b). The red spots (dotted line) showing $^{207}Pb/^{206}Pb$ ages of 2240–2243 Ma, 2192–2195 Ma and 1866–1878 Ma are not involved in the calculation of the mean $^{207}Pb/^{206}Pb$ age in (b).

Complex $^{207}Pb/^{206}Pb$ ages are obtained, which can be divided into four groups of 2240–2243 Ma (two analyses), 2192–2195 Ma (five analyses), 2167–2174 Ma (thirteen analyses) and 1866–1878 Ma (two analyses) (Table 1 and Fig. 5b). The zircons having the oldest ages are subhedral with weak oscillatory zoning (Fig. 4b), consistent with the detrital zircons recorded in the local and regional Paleoproterozic successions (e.g., Lan et al., 2014a; Wan et al., 2006). The zircons dated at 2192–2195 Ma (Figs. 4b and 5b) are gray with moderate oscillatory zoning, showing large similarities to those of the alkali-feldspar granite. Some anhedral and dark zircons have no oscillatory zoning or show mottled inner textures in CL images (Fig. 4b). They are characterized by the youngest $^{207}Pb/^{206}Pb$ ages of 1866–1878 Ma (Figs. 4b and 5b), which are similar to the metamorphic ages widely recorded in the Paleoproterozic successions (e.g., Tam et al., 2011; Wan et al., 2006; Zhou et al., 2008). The majorities of the zircons are gray to dark with moderate oscillatory zoning. They have a weighted mean $^{207}Pb/^{206}Pb$ age of 2171 ± 10 Ma (2σ), although some of them may experience variable amounts of Pb loss (Fig. 5b). Since the zircons of 2240–2243 Ma and 2192–2195 Ma are well in agree with those of the wallrocks, they are considered to be inherited zircons. The zircons of 1866–1878 Ma, however, are interpreted as metamorphic zircons, as strongly suggested by their mottled inner textures or none-oscillatory textures (Fig. 4b) as well as the gneissic structure of the host granite and the similar metamorphic ages widely recorded in the Jiao-Liao-Ji Belt. Finally, the weighted mean $^{207}Pb/^{206}Pb$ age of 2171 ± 10 Ma from the major zircons is regarded as the intrusive age of the albite granite.

5.2. Mineral chemistry

Quartz, feldspar and biotite are the major minerals in the alkali-feldspar granite and the albite granite. All the feldspars from the two types of granites are depleted in CaO, and therefore alkali-feldspars are dominant in these rocks. However, feldspars of the alkali-feldspar granite are either enriched in K_2O (Or_{93-95}) or enriched in Na_2O (An_{9-14}) (Table 2), which can be classified as orthoclase and albite to oligoclase (Fig. 6). In contrast, the feldspars from the albite granite are only enriched in Na_2O (An_{1-4}) (Table 2), and thus albite is dominant in the albite granite. Notably, the albites in the albite granite show less CaO contents than those in the alkali-feldspar granite (Fig. 6).

Biotites have distinct compositions between the alkali-feldspar granite and the albite granite. Much higher FeO and TiO_2 contents occur in the biotites of the alkali-feldspar granite, whereas MgO and Al_2O_3 are more abundant in the albite granite (Table 3). Based on the nomenclature of micas recommended by Tischendorf et al. (2001), the biotites of the alkali-feldspar granite are classified as Fe biotite while those of the albite granite show Mg biotite affinities.

Table 1
LA–ICP-MS zircon U–Pb data for the alkali-feldspar granite and the albite granite.

Spot	Concentrations (ppm)				Isotopic ratios						Isotopic ages (Ma)					
	Pb	Th	U	Th/U	$^{207}Pb/^{206}Pb$	1σ	$^{207}Pb/^{235}U$	1σ	$^{206}Pb/^{238}U$	1σ	$^{207}Pb/^{206}Pb$	1σ	$^{207}Pb/^{235}U$	1σ	$^{206}Pb/^{238}U$	1σ
CY2-92 (Alkali-feldspar granite)																
1	110	119	197	0.60	0.1371	0.0048	8.0826	0.2992	0.4211	0.0062	2192	59	2240	33	2266	28
2	150	144	272	0.53	0.1373	0.0048	8.0589	0.2714	0.4219	0.0055	2194	61	2238	30	2269	25
3	104	107	193	0.55	0.1377	0.0043	7.9205	0.2397	0.4133	0.0054	2198	54	2222	27	2230	25
4	157	152	292	0.52	0.1372	0.0041	7.9037	0.2277	0.4134	0.0049	2192	52	2220	26	2230	22
5	162	194	291	0.67	0.1375	0.0046	7.8279	0.2455	0.4096	0.0054	2196	58	2211	28	2213	25
6	114	114	216	0.53	0.1376	0.0049	7.8804	0.2657	0.4112	0.0059	2198	62	2217	30	2220	27
7	153	160	288	0.56	0.1370	0.0044	7.8551	0.2350	0.4077	0.0051	2191	28	2215	27	2205	23
8	158	202	288	0.70	0.1373	0.0049	7.9236	0.2680	0.4087	0.0052	2194	62	2222	31	2209	24
9	265	329	482	0.68	0.1373	0.0049	8.0422	0.2704	0.4120	0.0052	2194	61	2236	30	2224	24
10	108	107	197	0.54	0.1374	0.0060	8.3633	0.3432	0.4269	0.0063	2195	75	2271	37	2292	28
11	182	173	348	0.50	0.1374	0.0063	8.2012	0.3508	0.4190	0.0066	2195	80	2253	39	2256	30
12	169	199	308	0.64	0.1372	0.0056	7.9760	0.3022	0.4113	0.0055	2192	71	2228	34	2221	25
13	713	826	1346	0.61	0.1367	0.0049	8.0563	0.2826	0.4154	0.0071	2185	63	2237	32	2239	32
14	96	114	176	0.65	0.1374	0.0050	7.8990	0.2780	0.4083	0.0055	2194	64	2220	32	2207	25
15	146	179	269	0.67	0.1377	0.0053	7.9362	0.2920	0.4118	0.0062	2198	67	2224	33	2223	28
16	116	114	207	0.55	0.1373	0.0055	8.1497	0.3199	0.4248	0.0064	2194	70	2248	36	2282	29
17	114	126	210	0.60	0.1371	0.0054	7.8142	0.2891	0.4102	0.0067	2191	69	2210	33	2216	31
18	152	134	293	0.46	0.1371	0.0045	7.9178	0.2598	0.4130	0.0064	2191	57	2222	30	2228	29
19	352	337	645	0.52	0.1369	0.0036	8.2141	0.2134	0.4277	0.0043	2189	46	2255	24	2295	19
20	158	174	291	0.60	0.1373	0.0040	8.0225	0.2382	0.4180	0.0065	2194	50	2234	27	2251	29
21	192	250	337	0.74	0.1371	0.0036	8.0355	0.2096	0.4181	0.0048	2191	45	2235	24	2252	22
22	110	115	198	0.58	0.1371	0.0031	8.1979	0.1879	0.4278	0.0048	2190	40	2253	21	2296	22
CY2-43 (Albite granite)																
1	77	85	150	0.57	0.1413	0.0035	8.1152	0.2084	0.4159	0.0048	2243	44	2244	23	2242	22
2	195	75	776	0.10	0.1356	0.0031	4.1552	0.1014	0.2215	0.0022	2172	39	1665	20	1290	12
3	483	592	883	0.67	0.1352	0.0024	7.9112	0.1424	0.4227	0.0031	2169	31	2221	16	2273	14
4	151	219	286	0.77	0.1372	0.0031	7.7467	0.2029	0.4089	0.0076	2192	39	2202	24	2210	35
5	65	33	148	0.23	0.1353	0.0045	7.0679	0.2719	0.3768	0.0062	2168	58	2120	34	2061	29
6	49	52	96	0.54	0.1356	0.0035	7.5670	0.2038	0.4026	0.0046	2172	45	2181	24	2181	21
7	271	223	553	0.40	0.1354	0.0026	7.5520	0.1461	0.4019	0.0033	2169	33	2179	17	2178	15
8	1915	4405	3398	1.30	0.1352	0.0025	7.4923	0.1365	0.4004	0.0043	2169	31	2172	16	2171	20
9	37	54	70	0.76	0.1356	0.0033	7.5628	0.1827	0.4025	0.0042	2173	43	2180	22	2180	19
10	53	60	101	0.59	0.1411	0.0037	8.1138	0.2040	0.4153	0.0041	2240	46	2244	23	2239	19
11	895	1863	2236	0.83	0.1141	0.0026	4.8796	0.1138	0.3075	0.0031	1866	41	1799	20	1728	15
12	134	168	265	0.63	0.1356	0.0027	7.6101	0.1499	0.4033	0.0033	2172	35	2186	18	2184	15
13	436	616	763	0.81	0.1354	0.0025	8.2278	0.1615	0.4374	0.0045	2169	38	2256	18	2339	20
14	299	392	576	0.68	0.1358	0.0027	7.7189	0.1581	0.4090	0.0040	2174	35	2199	18	2211	18
15	374	517	622	0.83	0.1344	0.0030	8.2371	0.1769	0.4411	0.0036	2167	39	2257	19	2356	16
16	37	36	73	0.50	0.1373	0.0045	7.7368	0.2526	0.4096	0.0087	2194	58	2201	29	2213	40
17	228	195	730	0.27	0.1149	0.0044	3.8395	0.1287	0.2425	0.0043	1878	70	1601	27	1399	22
18	241	300	461	0.65	0.1357	0.0027	7.5774	0.1479	0.4025	0.0039	2174	35	2182	18	2180	18
19	298	371	568	0.65	0.1372	0.0025	7.7638	0.1364	0.4076	0.0028	2194	31	2204	16	2204	13
20	397	624	631	0.99	0.1373	0.0024	8.5515	0.1506	0.4491	0.0034	2194	31	2291	16	2391	15
21	218	235	534	0.44	0.1356	0.0025	6.3276	0.1273	0.3360	0.0035	2172	33	2022	18	1868	17
22	59	82	110	0.75	0.1375	0.0032	7.8082	0.1869	0.4096	0.0041	2195	41	2209	22	2213	19

5.3. Major and trace elements

Major and trace elements analyses are presented in Table 4. Both the alkali-feldspar granite and the albite granite have high SiO_2 (76.0–78.3 wt.%) and $K_2O + Na_2O$ (6.59–8.73 wt.%) contents, which thus classify the two rocks into alkali granite in the R1–R2 discrimination diagram (Fig. 7a). It is noteworthy that high K_2O (4.76–5.14 wt.%) and Na_2O (4.76–5.14 wt.%) compositions are simultaneously featured in the alkali-feldspar granite, whereas remarkably lower K_2O (0.29–0.44 wt.%) and higher Na_2O (6.15–6.56 wt.%) contents are distinctive in the albite granite. Further classification by An–Ab–Or diagram (Barker, 1979) shows that the alkali-feldspar belongs to granite, whereas the albite granite is classified as trondhjemite (Fig. 7b). However, the nearly pure albite (Ab > 96), the markedly low CaO (≤0.7 wt.%) and Al_2O_3 (≤12 wt.%) contents and the extremely high Na_2O/K_2O ratios (14–23) in the albite granite are significantly different from the typical trondhjemites (in trondhjemites, plagioclase is usually represented by oligoclase or andesine, CaO and Al_2O_3 contents are commonly higher than 1.5 wt.% and 14 wt.% respectively, Barker, 1979; Glikson, 1979). The alkali-feldspar granite has higher $Fe_2O_3{}^t$ and lower MgO contents ($Fe_2O_3{}^t$ = 1.67–2.20 wt.%, MgO = 0.17–0.26 wt.%) than those of the albite granite ($Fe_2O_3{}^t$ = 0.97–1.39 wt.%, MgO = 0.39–0.58 wt.%). Notably, the Mg# value of the alkali-feldspar granite (17–20) is much lower than that of the albite granite (44–45). Other major elements such as Al_2O_3 (11.6–12.3 wt.%), CaO (0.39–0.75 wt.%), TiO_2 (0.24–0.29 wt.%) and P_2O_5 (0.02–0.03 wt.%) show no systematical difference between the two types of rocks. These rocks are chemically metaluminous to peraluminous (Fig. 7c), and fall into the alkaline field in the SiO_2-A.R. diagram (Fig. 7d).

The alkali-feldspar granite and the albite granite are characterized by similar REE distribution patterns, which show moderate fractionation between LREE and HREE ($(La/Yb)_N$ = 7.0–17.7) and have strong negative Eu anomalies (δEu = 0.24–0.45) (Table 4 and Fig. 8). However, the HREE contents of the albite granite (25.2–27.1 ppm) are higher than those of the alkali-feldspar granite (16.3–22.3 ppm) (Fig. 8b). All the rocks are significantly depleted in HFSEs of Nb, Ta, P and Ti. In addition, they also show depletion in LILEs of Sr and Ba. Furthermore, Rb and Ba depletion in the albite granite is much more impressive (Fig. 8a).

Table 2
Representative electron microprobe analyses of feldspar for the alkali-feldspar granite and the albite granite.

Granite	Alkali-feldspar granite											Albite granite								
Sample	CY2-49			CY2-75				CY2-92				CY2-43			CY2-44					
Mineral	Albite		Oligoclase	K-feldspar		K-feldspar		Oligoclase		Albite	K-feldspar			Albite				Albite		
SiO_2	66.7	66.1	66.6	65.1	64.5	64.8	65.1	65.4	65.4	66.4	68.3	65.7	65.2	64.6	65.1	68.9	68.5	68.3	68.8	68.9	68.8	67.6	68.0
Al_2O_3	19.3	20.8	19.9	21.0	17.5	18.0	18.0	18.0	17.6	21.2	20.5	19.7	17.8	17.8	17.6	19.3	19.5	19.5	19.6	18.9	19.7	19.7	19.5
CaO	1.95	2.01	1.94	2.43	0.00	0.00	0.00	0.00	0.02	2.87	2.35	1.01	0.00	0.03	0.00	0.67	0.73	0.66	0.74	0.31	0.57	0.77	0.68
Na_2O	11.0	10.3	10.32	10.09	0.68	0.51	0.72	0.62	0.46	9.97	10.1	10.9	0.39	0.52	0.23	0.47	11.5	11.6	11.6	11.7	11.6	11.6	10.9
K_2O	0.13	0.10	0.21	0.10	15.9	16.0	15.6	15.4	15.8	0.15	0.14	0.06	15.9	15.6	16.1	15.9	0.10	0.06	0.05	0.07	0.03	0.06	0.07
Total	99.1	99.3	99.0	98.7	98.6	99.3	99.5	99.3	99.2	99.7	99.5	100.0	99.8	99.1	98.6	99.1	100.5	100.3	100.1	100.8	99.9	100.7	99.7	99.2
%Ab	0.90	0.90	0.90	0.88	0.06	0.05	0.07	0.06	0.04	0.86	0.88	0.95	0.04	0.05	0.02	0.04	0.96	0.96	0.97	0.98	0.97	0.96	0.96
%An	0.09	0.10	0.09	0.12	0.00	0.00	0.00	0.00	0.00	0.14	0.11	0.05	0.00	0.00	0.00	0.00	0.03	0.03	0.03	0.01	0.03	0.04	0.03
%Or	0.01	0.01	0.01	0.01	0.93	0.95	0.93	0.94	0.95	0.01	0.01	0.00	0.96	0.95	0.97	0.95	0.01	0.00	0.00	0.00	0.00	0.00	0.00

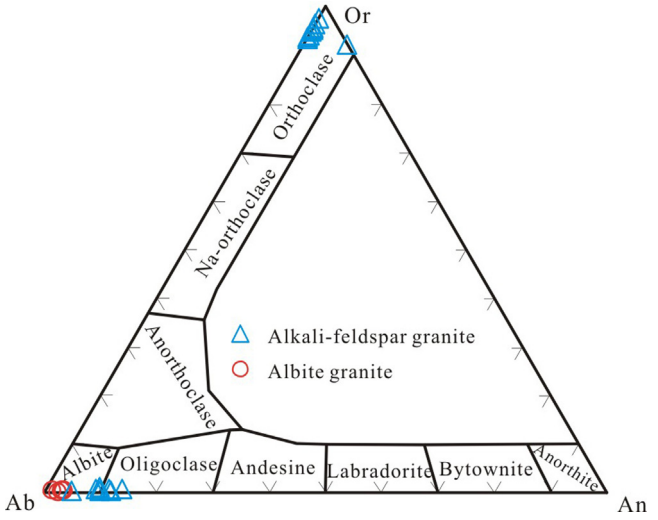

Fig. 6. Classification of feldspar from the alkali-feldspar granite and the albite granite.

5.4. Sr–Nd–Hf isotopes

The alkali-feldspar granite has high Rb (121–156 ppm) and low Sr (60.9–140 ppm) contents, and thus show remarkably high $^{87}Rb/^{86}Sr$ (2.5531–7.5484) and $^{87}Sr/^{86}Sr$ (0.781999–0.919311) ratios (Table 5). When calculated back to the intrusive age of 2193 Ma, the initial $^{87}Sr/^{86}Sr$ ratios are very low (0.671524–0.701244), even lower than those of the mantle reservoirs (e.g., Hofmann, 1997; Zindler and Hart, 1986). Since the age-corrected $^{87}Sr/^{86}Sr$ ratios may bear large uncertainties for high Rb/Sr rocks, the correction probably yields unreasonably low $^{87}Sr/^{86}Sr$ ratios of less than 0.700, which cannot be used in petrogenetic discussions (Wu et al., 2002). In contrast, the albite granite is characterized by low Rb (8.34–12.2 ppm) and high Sr (68.5–117 ppm) contents, and therefore shows low $^{87}Rb/^{86}Sr$ (0.3021–0.3527) and $^{87}Sr/^{86}Sr$ (0.713940–0.716467) ratios. The initial $^{87}Sr/^{86}Sr$ ratios (t = 2171 Ma) of the albite granite vary between 0.704482 and 0.705424.

Low Sm (5.72–7.25 ppm) and high Nd (35.6–51.3 ppm) contents are present in the alkali-feldspar granite, leading to the $^{147}Sm/^{144}Nd$ and $^{143}Nd/^{144}Nd$ ratios varying from 0.0926 to 0.0972 and from 0.510881 to 0.510969, respectively (Table 5). The $\varepsilon_{Nd}(t)$ values range from −5.3 to −4.6. The Sm–Nd isotopic compositions of the albite granite are similar to those of the alkali-feldspar granite, which show Sm and Nd contents of 5.06–8.40 ppm and 30.7–53.3 ppm, and $^{147}Sm/^{144}Nd$ and $^{143}Nd/^{144}Nd$ ratios of 0.0954–0.0997 and 0.510956–0.511028, respectively. The $\varepsilon_{Nd}(t)$ values vary from −4.6 to −4.4, also falling into the range of the alkali-feldspar granite. Both the alkali-feldspar granite and the albite granite have ancient two-stage Nd depleted mantle model ages (T_{DM2}), of which the alkali-feldspar granite has T_{DM2} of 2983–3051 Ma (averaging at 2999 Ma) and the albite granite has T_{DM2} of 2944–2961 Ma (averaging at 2953 Ma).

The Hf isotopic compositions are listed in Table 6. Twenty-two analyses from the alkali-feldspar granite (represented by the sample of CY2-92) yield $^{176}Hf/^{177}Hf$ ratios of 0.281242–0.281315 and $\varepsilon_{Hf}(t)$ varying from −6.7 to −4.3 with an average value of −5.6. Similar results are obtained from the albite granite, which show $^{176}Hf/^{177}Hf$ ratios of 0.281258–0.281444 and $\varepsilon_{Hf}(t)$ ranging from −7.0 to −3.8 with an average value of −5.7. The two-stage Hf depleted mantle model ages (T_{DM2}) of the zircons from the alkali-feldspar granite and the albite granite change from 3030 Ma to 3179 Ma (averaging at 3107 Ma) and from 2979 to 3177 Ma (averaging at 3096 Ma), respectively.

Table 3
Representative electron microprobe analyses of biotite for the alkali-feldspar granite and the albite granite.

Granite	Alkali-feldspar granite										Albite granite						
Sample	CY2-49				CY2-75						CY2-43			CY2-44			
SiO_2	37.4	37.8	37.5	38.0	35.4	36.2	35.2	36.1	36.0	36.9	37.9	37.7	37.6	38.4	38.2	38.8	38.3
TiO_2	3.14	3.00	3.09	2.90	3.20	3.60	3.76	3.00	2.99	3.35	2.07	2.02	2.00	2.17	2.20	1.97	1.87
Al_2O_3	14.8	14.8	14.9	15.4	15.8	15.4	16.6	16.6	16.0	14.9	16.7	16.6	17.2	17.0	17.0	17.0	17.5
FeO	22.0	21.8	23.5	20.6	28.0	27.6	27.6	26.5	27.3	27.6	15.4	15.3	15.8	16.5	16.3	17.0	16.7
MnO	0.32	0.34	0.33	0.19	0.23	0.30	0.25	0.33	0.25	0.22	0.17	0.14	0.14	0.18	0.14	0.18	0.20
MgO	8.54	8.73	7.20	9.13	4.15	4.27	3.97	4.77	5.00	4.88	12.6	13.4	13.2	12.5	12.9	12.2	11.9
CaO	0.00	0.00	0.00	0.00	0.00	0.00	0.00	0.00	0.04	0.00	0.01	0.00	0.00	0.00	0.00	0.00	0.00
Na_2O	0.19	0.15	0.35	0.20	0.14	0.26	0.07	0.12	0.09	0.09	0.25	0.23	0.16	0.31	0.14	0.17	0.28
K_2O	9.75	9.74	9.42	9.76	9.61	9.36	9.70	9.20	8.75	9.49	9.53	9.27	9.45	9.65	9.88	9.82	10.0
Total	97.4	97.5	97.4	97.6	97.1	97.4	97.8	97.1	97.0	97.5	94.6	94.9	95.7	97.0	97.3	97.5	97.2
Cations normalized to 22 oxygens																	
Si	5.74	5.77	5.77	5.77	5.58	5.64	5.50	5.60	5.62	5.72	5.69	5.65	5.60	5.66	5.63	5.71	5.66
Ti	0.36	0.34	0.36	0.33	0.38	0.42	0.44	0.35	0.35	0.39	0.23	0.23	0.22	0.24	0.24	0.22	0.21
^{T}Al	2.67	2.66	2.70	2.75	2.94	2.84	3.06	3.05	2.94	2.72	2.95	2.92	3.01	2.96	2.95	2.95	3.04
Fe^{2+}	2.82	2.78	3.01	2.61	3.68	3.60	3.60	3.44	3.56	3.58	1.93	1.92	1.96	2.03	2.01	2.08	2.06
Mn	0.04	0.04	0.04	0.02	0.03	0.04	0.03	0.04	0.03	0.03	0.02	0.02	0.02	0.02	0.02	0.02	0.03
Mg	1.95	1.99	1.65	2.06	0.97	0.99	0.92	1.11	1.16	1.13	2.81	2.99	2.92	2.74	2.83	2.67	2.63
Ca	0.00	0.00	0.00	0.00	0.00	0.00	0.00	0.00	0.01	0.00	0.00	0.00	0.00	0.00	0.00	0.00	0.00
Na	0.06	0.04	0.10	0.06	0.04	0.08	0.02	0.04	0.03	0.03	0.07	0.07	0.05	0.09	0.04	0.05	0.08
K	1.91	1.90	1.85	1.89	1.93	1.86	1.93	1.82	1.74	1.88	1.82	1.77	1.80	1.82	1.86	1.84	1.89
$Mg^{\#}$	0.41	0.42	0.35	0.44	0.21	0.22	0.20	0.24	0.25	0.24	0.59	0.61	0.60	0.57	0.58	0.56	0.56
P(kb)	1.55	1.54	1.66	1.80	2.37	2.07	2.73	2.70	2.38	1.71	2.42	2.33	2.60	2.44	2.42	2.40	2.69

$Mg^{\#} = Mg/(Mg + Fe)$, $P\,(kb) = 3.03 \times {}^{T}Al - 6.53$.

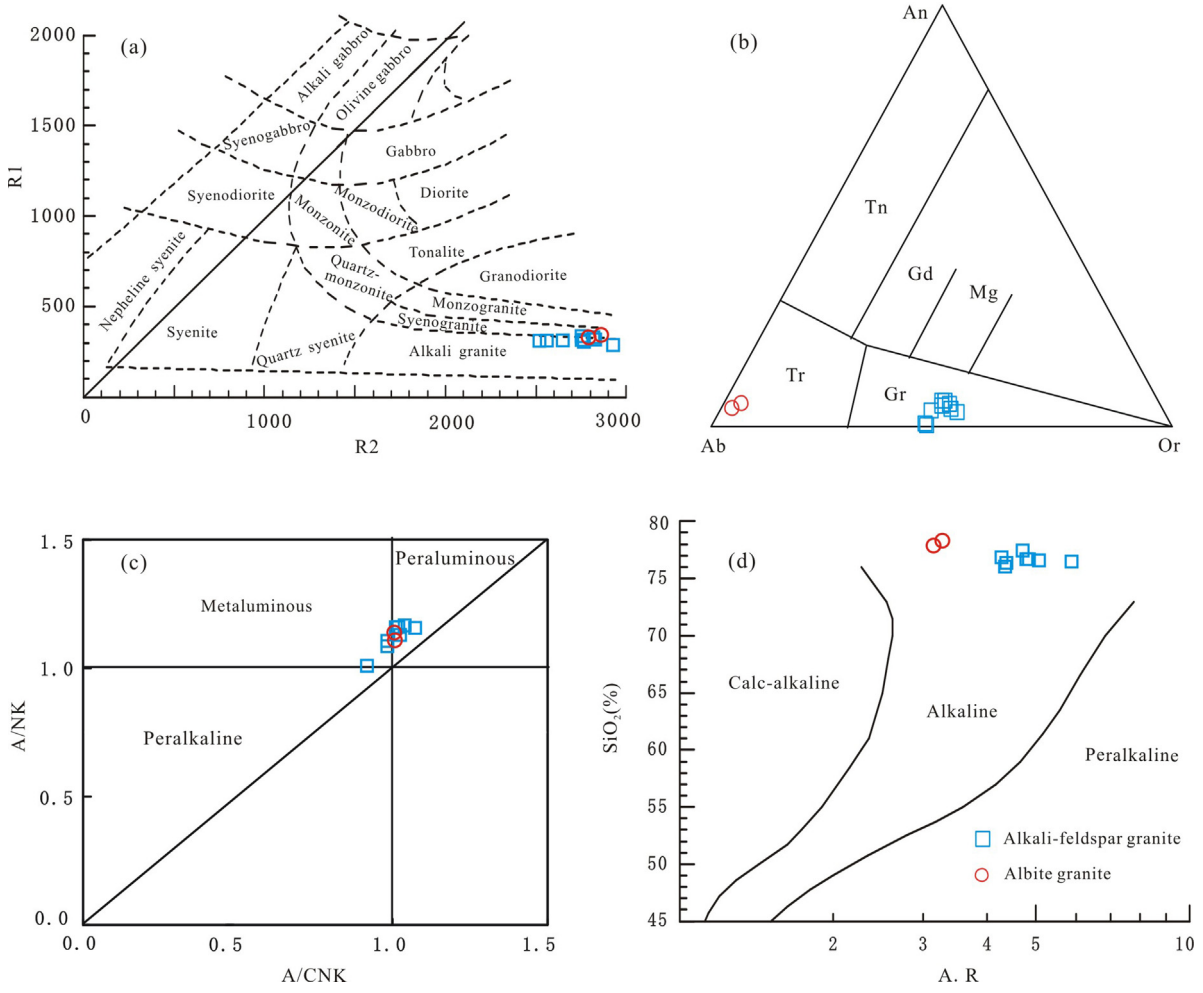

Fig. 7. Plots of R1 vs. R2 [R1 = 4Si−11(Na + K)−2(Fe + Ti), R2 = 6Ca + 2Mg + Al] (a), A/NK [molar ratio $Al_2O_3/(Na_2O + K_2O)$] vs. A/CNK [molar ratio $Al_2O_3/(CaO + Na_2O + K_2O)$] (b), An–Ab–Or (c) and SiO_2 vs. A.R [$Al_2O_3 + CaO + (Na_2O + K_2O)$]/[$Al_2O_3 + CaO - (Na_2O + K_2O)$] (d) for the alkali-feldspar granite and the albite granite. (a) is from De la Roche et al. (1980), (b) is from Barker (1979) and (d) is from Wright (1969).

Table 4
Major oxides (wt.%) and trace elements (ppm) data for the alkali-feldspar granite and the albite granite.

Rock-type	Alkali-feldspar granite									Albite granite		GSR1	GSR1
Sample	CY2-49	CY2-75	CY2-76	CY2-77	CY2-78	CY2-79	CY2-80	CY2-86	CY2-92	CY2-43	CY2-44	Meas.	Refer.
SiO_2	76.0	76.3	76.6	76.6	76.7	76.4	76.6	76.4	77.4	78.3	77.9	73.1	72.8
TiO_2	0.28	0.27	0.24	0.25	0.27	0.28	0.26	0.28	0.24	0.29	0.26	0.28	0.28
Al_2O_3	12.0	11.9	11.6	11.7	12.0	11.8	11.9	11.8	11.6	12.3	12.0	13.4	13.4
$Fe_2O_3^t$	2.07	2.20	2.00	2.02	1.67	2.17	1.91	2.14	1.84	0.97	1.39	2.13	2.14
FeO	1.21	1.47	1.09	1.00	0.93	1.49	1.12	1.10	1.34	0.72	1.04		
MnO	0.01	0.01	0.02	0.02	0.01	0.02	0.02	0.01	0.02	0.01	0.01	0.06	0.06
MgO	0.26	0.24	0.23	0.21	0.17	0.26	0.20	0.22	0.23	0.39	0.58	0.41	0.42
CaO	0.73	0.64	0.58	0.62	0.57	0.75	0.53	0.69	0.39	0.57	0.70	1.54	1.55
Na_2O	3.11	2.98	3.73	3.75	3.54	3.10	3.05	3.23	2.86	6.56	6.15	3.11	3.13
K_2O	4.89	4.90	4.88	4.98	4.92	4.76	5.14	4.93	4.97	0.29	0.44	5.02	5.01
P_2O_5	0.03	0.03	0.03	0.03	0.03	0.03	0.03	0.03	0.03	0.02	0.03	0.09	0.09
LOI	0.30	0.38	0.40	0.22	0.40	0.46	0.26	0.42	0.52	0.40	0.42	0.69	0.69
Total	99.7	99.9	100.3	100.4	100.3	100.1	99.9	100.1	100.2	100.1	99.9	99.8	99.6
$Mg^{\#}$	19.9	17.8	18.5	17.1	16.8	19.2	17.2	16.9	19.8	44.3	45.2		
A/CNK	1.02	1.04	0.93	0.92	0.99	1.02	1.03	0.99	1.08	1.01	1.01		
A/NK	1.15	1.16	1.01	1.01	1.08	1.15	1.12	1.10	1.15	1.10	1.13		
CIA	50.6	51.1	48.0	47.9	49.6	50.4	50.7	49.6	51.9	50.2	50.3		
Li	8.40	7.33	4.77	2.65	4.91	6.20	4.94	3.06	8.03	1.91	9.47	129	131
Be	2.01	1.93	1.95	1.82	2.06	1.88	2.06	1.73	1.75	0.69	1.23	12.2	12.4
Sc	4.66	4.26	4.12	3.98	4.01	4.44	4.11	2.94	3.95	2.16	3.48	6.01	6.10
V	11.0	8.83	8.88	8.12	8.98	9.21	8.10	8.33	9.73	6.31	8.84	23.7	24.0
Cr	209	213	245	162	245	266	211	215	239	240	245	4.78	5.00
Co	4.17	3.72	4.32	3.29	3.72	4.69	3.44	3.54	3.84	2.91	3.39	3.35	3.40
Ni	7.41	7.08	8.85	3.71	5.24	6.01	6.77	5.24	9.97	2.74	0.30	2.37	2.30
Cu	2.05	3.64	5.37	1.81	5.64	1.89	2.33	1.90	7.54	2.41	2.25	2.40	3.20
Zn	10.3	11.5	20.8	24.2	14.0	17.5	29.1	12.6	13.9	11.5	17.0	27.6	28.0
Ga	15.7	14.6	15.1	16.0	16.4	16.3	15.8	15.1	15.4	12.5	13.8	19.1	19.0
Rb	126	127	148	152	147	134	154	134	121	9.16	13.0	465	466
Sr	141	123	70.3	63.3	65.0	86.9	64.0	70.3	66.6	74.6	118	109	106
Cs	1.21	1.36	2.31	1.74	2.02	1.70	3.08	1.62	0.63	0.45	0.73	38.2	38.4
Ba	1254	1123	1121	1026	1025	1071	1080	1019	995	31.0	51.6	343	343
Nb	17.0	16.7	15.8	16.3	17.8	18.2	16.3	17.6	15.2	20.5	21.0	38.5	40.0
Ta	1.30	1.26	1.33	1.29	1.39	1.47	1.23	1.27	1.29	1.48	1.51	7.36	7.20
Zr	297	318	296	295	271	269	293	298	213	317	321	164	167
Hf	8.86	9.58	9.14	9.12	8.52	8.34	8.70	8.90	6.94	9.71	10.0	6.35	6.30
La	63.9	64.6	71.7	54.6	64.1	64.1	55.6	60.7	48.3	48.8	84.8	54.7	54.0
Ce	125	122	136	102	119	123	106	101	90.6	95.4	159	109	108
Pr	14.4	14.2	15.7	12.0	13.9	14.3	12.3	13.3	10.7	11.3	18.4	13.3	12.7
Nd	50.2	49.5	51.5	42.0	48.0	47.8	42.8	45.8	37.7	40.0	63.5	47.4	47.0
Sm	7.60	7.29	8.04	6.54	6.96	7.58	6.47	6.71	5.74	6.68	9.52	9.75	9.70
Eu	0.71	0.67	0.72	0.61	0.64	0.70	0.62	0.61	0.82	0.51	0.83	0.83	0.85
Gd	6.30	6.36	7.00	5.79	5.76	6.49	5.51	5.84	5.27	6.22	8.45	9.37	9.30
Tb	0.91	0.87	0.99	0.87	0.78	0.97	0.85	0.83	0.75	1.00	1.22	1.63	1.65
Dy	5.03	4.59	5.38	5.02	3.99	5.65	4.65	4.71	3.91	6.13	6.82	10.1	10.2
Ho	1.01	0.90	1.07	1.08	0.83	1.20	0.95	0.95	0.79	1.41	1.40	2.10	2.05
Er	2.82	2.44	3.01	3.02	2.34	3.39	2.59	2.80	2.28	4.34	4.04	6.34	6.50
Tm	0.44	0.37	0.47	0.48	0.37	0.54	0.41	0.44	0.37	0.71	0.62	1.03	1.06
Yb	2.89	2.46	3.07	3.18	2.51	3.51	2.68	2.95	2.53	4.73	3.96	7.31	7.40
Lu	0.44	0.38	0.47	0.48	0.39	0.54	0.41	0.46	0.39	0.69	0.61	1.12	1.15
Y	24.7	21.5	27.3	27.3	20.7	30.7	22.4	25.6	20.0	35.8	35.4	59.0	62.0
Tl	0.57	0.54	0.68	0.65	0.65	0.60	0.71	0.59	0.60	0.07	0.09	1.99	1.93
Pb	9.52	12.2	19.1	17.8	17.3	18.6	21.1	14.5	12.8	8.22	9.25	32.0	31.0
Bi	0.04	0.07	0.05	0.04	0.11	0.07	0.14	0.05	0.06	0.00	0.01	0.55	0.53
Th	15.9	16.1	18.5	15.3	16.6	19.0	15.4	15.7	13.2	17.7	20.6	54.9	54.0
U	2.48	3.45	3.01	3.13	3.21	4.17	3.29	3.24	3.51	2.67	3.56	18.9	18.8
Nb/Ta	13.1	13.3	11.9	12.6	12.8	12.4	13.2	13.9	11.8	13.9	13.9		
T_{zr}(°C)	847	856	834	833	834	837	846	843	823	852	853		
δEu	0.30	0.30	0.29	0.30	0.30	0.30	0.31	0.29	0.45	0.24	0.28		
$(La/Yb)_N$	14.9	17.7	15.7	11.6	17.3	12.3	14.0	13.9	12.9	7.00	14.4		

LOI: loss on ignition. $Mg^{\#} = 100 \times Mg/(Mg + \sum Fe)$ atomic ratio. $T_{Zr}(^{\circ}C) = 12{,}900/[2.95(0.85M) + \ln(496{,}000/Zr_{melt})]$, $M = (Na + K + 2Ca)/(Al \times Si)$ cation ratio (Watson and Harrison, 1983).CIA = molecular $(Al_2O_3/(Al_2O_3 + CaO + Na_2O + K_2O)) \times 100$. GSR1 is Chinese granite standard. Meas.: the actually measured value for reference standard. Refer.: recommended value for reference standard.

6. Discussion

6.1. Genetic type of the granites

During last thirty years, granitic rocks have been popularly divided into I-, S-, M- and A-types based on the nature of their protoliths (Bonin, 2007; Clarke, 1992; Pitcher, 1997; White, 1979). It appears that S-type granites are relatively easy to be identified, due to their distinctive mineral assemblages and chemical compositions. Generally, S-type granites are always oversaturated in Al or peraluminous (Mol. $Al_2O_3/(Na_2O + K_2O + CaO) > 1.1$) and therefore they commonly have alumino-silicates such as muscovite, garnet, cordierite (Chappell and White, 1974, 2001). These features, however, are not observed in the alkali-feldspar granite and the albite granite. M-type granites were considered to be derived from mantle conditions or mantle-derived sources (such as subducted oceanic

Table 5
Sr–Nd isotopic compositions of the alkali-feldspar granite and the albite granite.

Sample	Rock type	Age (Ma)	Rb (ppm)	Sr (ppm)	$^{87}Rb/^{86}Sr$	$^{87}Sr/^{86}Sr$	$\pm2\sigma$	$(^{87}Sr/^{86}Sr)_i$	Sm (ppm)	Nd (ppm)	$^{147}Sm/^{144}Nd$	$^{143}Nd/^{144}Nd$	$\pm2\sigma$	$\varepsilon_{Nd}(t)$	$f_{Sm/Nd}$	T_{DM1} (Ma)	T_{DM2} (Ma)
CY2-49	Alkali-feldspar granite	2193	122	140	2.5531	0.781999	11	0.701244	7.2	46.4	0.0936	0.510881	12	−5.3	−0.52	2863	3051
CY2-75			130	120	3.1502	0.799738	10	0.700096	7.3	47.4	0.0926	0.510908	11	−4.4	−0.53	2805	2983
CY2-78			144	62.4	6.7735	0.885773	13	0.671524	7.0	45.9	0.0929	0.510910	13	−4.5	−0.53	2809	2986
CY2-80			156	60.9	7.5484	0.919311	13	0.680552	6.6	41.3	0.0960	0.510958	11	−4.4	−0.51	2823	2983
CY2-86			143	81.7	5.1379	0.843272	12	0.680757	7.9	51.3	0.0929	0.510905	10	−4.6	−0.53	2816	2996
CY2-92			121	63.9	5.5672	0.850485	12	0.674393	5.7	35.6	0.0972	0.510969	10	−4.6	−0.51	2838	2994
CY2-43	Albite granite	2171	8.34	68.5	0.3527	0.716467	11	0.705424	5.06	30.7	0.0997	0.511028	12	−4.4	−0.49	2821	2944
CY2-44			12.2	117	0.3021	0.713940	11	0.704482	8.40	53.3	0.0954	0.510956	10	−4.6	−0.51	2811	2961

Chondrite Uniform Reservoir (CHUR) values ($^{87}Rb/^{86}Sr = 0.0847$, $^{87}Sr/^{86}Sr = 0.7045$, $^{147}Sm/^{144}Nd = 0.1967$, $^{143}Nd/^{144}Nd = 0.512638$) are used for the calculation. $\lambda_{Rb} = 1.42 \times 10^{-11}$ year^{-1}, $\lambda_{Sm} = 6.54 \times 10^{-12}$ year^{-1} (Lugmair and Harti, 1978).

crust or overlying mantle) and commonly show enrichment in basic elements (such as Cr, Ni, Co, V, Ti, Mg) and volcanic arc signatures (White, 1979; White and Chappell, 1983). The remarkably felsic features (SiO_2 > 75 wt.%, MgO < 0.60 wt.%) as well as the lack of volcanic arc signatures of the granites in this study indicate that they could not be M-type granite. I-type granites are generally metaluminous to weakly peraluminous with a wide range of SiO_2 contents (56–77 wt.%) (Chappell and White, 1974, 2001; Frost et al., 2001), which are consistent with some major element characteristics of the alkali-feldspar granite and the albite granite. However, the high SiO_2, $Na_2O + K_2O$, Zr, Nb, Ga, Y and REE (except Eu) contents coupled with the low CaO, Ba and Sr concentrations (Table 4 and Fig. 8) are distinct from I-type granites (Chappell and White, 1974, 2001; Whalen et al., 1987). Instead, they show large affinities to A-type granites (Whalen et al., 1987). Former studies have made great efforts to discriminate different types of granitoids using diagrams (e.g., Dall'Agnol and de Oliveira, 2007; Frost et al., 2001; Whalen et al., 1987). In the famous discrimination diagrams of Whalen et al. (1987), most samples of the alkali-feldspar granite and the albite granite are plotted in the field of A-type granite (Fig. 9). This is also confirmed by the criteria of Dall'Agnol and de Oliveira (2007) using the diagrams of $CaO/(FeO^t + MgO + TiO_2)$ vs. $(Al_2O_3 + CaO)$ and $CaO/(FeO^t + MgO + TiO_2)$ vs. Al_2O_3, which are effective in discriminating A-type granites from calc-alkaline granitoids (Fig. 10). Therefore, we consider that both the alkali-feldspar granite and the albite granite are A-type granite, although the latter shows remarkably low K_2O anomaly when compared with the classical A-type granites. This anomaly will be discussed below.

6.2. Sources of the granites

Numerous studies have shown that A-type granites can be derived from crust (Clemens et al., 1986; Collins et al., 1982; Creaser et al., 1991; King et al., 2001; Landenberger and Collins, 1996; Whalen et al., 1987), mantle (e.g., Turner et al., 1992; Litvinovsky et al., 2002; Mushkin et al., 2003; Namur et al., 2011) and crust–mantle interactions (e.g., Anderson et al., 2003; Bédard, 1990; Haapala et al., 2007; Harris et al., 1986; Kerr and Fryer, 1993; Martin, 2006; Yang et al., 2006), suggesting that the sources of A-type granites are diverse and should be carefully treated. The alkali-feldspar granite and the albite granite (SiO_2 = 76.3–78.3 wt.%) are more felsic than those of the classical A-type granites (averaging at SiO_2 = 73.8 wt.%, Whalen et al., 1987), which imply that involvement of felsic crustal materials or strong fractionation of mafic melts may have occurred during their formation. Extreme fractionation of basaltic melts (the amount of fractionation >90%) has been proved to be an applicable way to generate highly felsic A-type granites (e.g., Mushkin et al., 2003; Turner et al., 1992; Namur et al., 2011). Such A-type granites are commonly associated with large-scale mafic rocks and show wide variation of major elements (e.g., Mushkin et al., 2003; Namur et al., 2011). However, no mafic rocks or mafic enclaves spatially and temporally associated with the alkali-feldspar granite and the albite granite indicate the minor possibility of mafic melts involvement. In addition, although limited fractionation of plagioclase probably occurred (Fig. 11a and b), the relatively homogeneous compositions of major elements and the indistinctive covariation between SiO_2 and MgO, Mg#, $Fe_2O_3^t$ and TiO_2 (Fig. 11c–f) preclude significant fractionation of mafic minerals from basaltic magmas to granitic melts, illustrating that extreme fractionation of mantle-derived mafic melts could not be the case for the generation of the A-type granites in this study. Crust–mantle interactions, including mantle-derived melts coupled with crustal assimilation and crystal fractionation (AFC process, e.g., Anderson et al., 2003; Barboni and Bussy, 2013), magma mixing between mantle- and crust-derived melts (e.g., Bédard, 1990; Haapala et al., 2007; Kerr and Fryer,

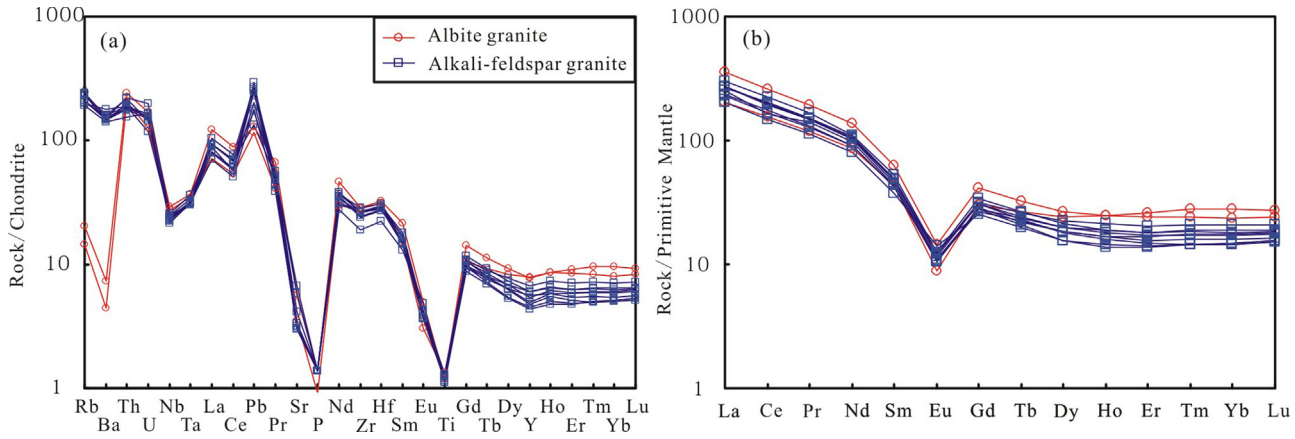

Fig. 8. Chondrite-normalized REE distribution patterns (a) and Primitive Mantle normalized trace element diagrams (b) for the alkali-feldspar granite and the albite granite. The chondrite and PM values are from Sun and McDonough (1989).

Table 6
LA-ICP-MS zircon Hf isotopic data for the alkali-feldspar granite and the albite granite.

Spot No.	Age (Ma)	$^{176}Yb/^{177}Hf$	$^{176}Lu/^{177}Hf$	$^{176}Hf/^{177}Hf$	2σ	$(^{176}Hf/^{177}Hf)_i$	$\varepsilon_{Hf}(0)$	$\varepsilon_{Hf}(t)$	T_{DM1} (Ma)	T_{DM2} (Ma)	$f_{Lu/Hf}$
CY2-92 (Alkali-feldspar granite)											
1	2192	0.0440	0.0012	0.281268	0.000017	0.281218	−53.2	−6.0	2783	3131	−0.96
2	2194	0.0280	0.0007	0.281256	0.000015	0.281225	−53.6	−5.7	2767	3116	−0.98
3	2200	0.0252	0.0007	0.281274	0.000014	0.281245	−53.0	−4.9	2739	3068	−0.98
4	2194	0.0294	0.0008	0.281258	0.000016	0.281223	−53.5	−5.8	2771	3120	−0.97
5	2198	0.0492	0.0013	0.281263	0.000015	0.281210	−53.4	−6.1	2795	3146	−0.96
6	2198	0.0417	0.0012	0.281246	0.000023	0.281194	−54.0	−6.7	2816	3179	−0.96
7	2192	0.0347	0.0010	0.281268	0.000024	0.281227	−53.2	−5.7	2768	3113	−0.97
8	2194	0.0357	0.0010	0.281281	0.000018	0.281237	−52.7	−5.3	2755	3089	−0.97
9	2194	0.0514	0.0013	0.281302	0.000015	0.281246	−52.0	−4.9	2746	3069	−0.96
10	2195	0.0280	0.0008	0.281251	0.000015	0.281219	−53.8	−5.9	2775	3127	−0.98
11	2195	0.0265	0.0007	0.281294	0.000016	0.281264	−52.3	−4.3	2714	3031	−0.98
12	2192	0.0367	0.0010	0.281251	0.000016	0.281210	−53.8	−6.3	2791	3150	−0.97
13	2194	0.1002	0.0025	0.281315	0.000018	0.281210	−51.5	−6.2	2816	3147	−0.92
14	2194	0.0378	0.0010	0.281277	0.000019	0.281235	−52.9	−5.4	2758	3095	−0.97
15	2198	0.0336	0.0010	0.281303	0.000016	0.281263	−51.9	−4.3	2718	3030	−0.97
16	2194	0.0235	0.0007	0.281265	0.000015	0.281237	−53.3	−5.3	2749	3089	−0.98
17	2191	0.0486	0.0013	0.281281	0.000016	0.281227	−52.7	−5.7	2772	3113	−0.96
18	2191	0.0237	0.0008	0.281242	0.000023	0.281211	−54.1	−6.3	2786	3149	−0.98
19	2189	0.0332	0.0009	0.281269	0.000015	0.281231	−53.2	−5.6	2762	3106	−0.97
20	2194	0.0537	0.0015	0.281299	0.000017	0.281237	−52.1	−5.2	2760	3088	−0.96
21	2191	0.0403	0.0012	0.281287	0.000022	0.281237	−52.5	−5.3	2757	3091	−0.96
22	2190	0.0328	0.0009	0.281265	0.000016	0.281227	−53.3	−5.7	2766	3113	−0.97
CY2-43 (Albite granite)											
1	2243	0.0607	0.0016	0.281626	0.000016	0.281558	−40.5	7.2	2316	2357	−0.95
2	2172	0.0400	0.0011	0.281260	0.000025	0.281215	−53.5	−6.6	2787	3152	−0.97
3	2169	0.0821	0.0022	0.281318	0.000020	0.281228	−51.4	−6.2	2786	3125	−0.93
4	2192	0.0483	0.0012	0.281287	0.000016	0.281235	−52.5	−5.4	2761	3095	−0.96
5	2168	0.1377	0.0033	0.281432	0.000019	0.281295	−47.4	−3.8	2709	2979	−0.90
6	2172	0.0454	0.0012	0.281276	0.000019	0.281226	−52.9	−6.2	2774	3128	−0.96
7	2169	0.1229	0.0032	0.281406	0.000017	0.281274	−48.3	−4.5	2737	3023	−0.90
8	2169	0.0754	0.0018	0.281313	0.000017	0.281237	−51.6	−5.9	2769	3106	−0.94
9	2173	0.0272	0.0007	0.281267	0.000016	0.281238	−53.2	−5.7	2749	3101	−0.98
10	2240	0.0615	0.0017	0.281655	0.000021	0.281584	−39.5	8.1	2279	2302	−0.95
12	2172	0.0536	0.0014	0.281260	0.000019	0.281203	−53.5	−7.0	2807	3177	−0.96
13	2169	0.0388	0.0010	0.281294	0.000019	0.281252	−52.3	−5.3	2734	3072	−0.97
14	2174	0.0433	0.0012	0.281258	0.000016	0.281209	−53.6	−6.7	2795	3163	−0.96
15	2167	0.0448	0.0011	0.281291	0.000017	0.281245	−52.4	−5.6	2746	3090	−0.97
16	2194	0.0447	0.0012	0.281203	0.000021	0.281151	−55.5	−8.3	2875	3275	−0.96
18	2174	0.0777	0.0023	0.281311	0.000021	0.281217	−51.7	−6.4	2803	3146	−0.93
19	2194	0.0786	0.0019	0.281357	0.000021	0.281276	−50.0	−3.9	2714	3004	−0.94
20	2194	0.0241	0.0007	0.281318	0.000017	0.281289	−51.4	−3.4	2680	2976	−0.98
21	2172	0.1244	0.0037	0.281444	0.000018	0.281292	−47.0	−3.8	2718	2983	−0.89
22	2195	0.0455	0.0012	0.281287	0.000021	0.281235	−52.5	−5.3	2760	3092	−0.96

The following parameters were applied to calculation: $(^{176}Lu/^{177}Hf)_{CHUR} = 0.0332$, $(^{176}Hf/^{177}Hf)_{CHUR,0} = 0.282772$, $(^{176}Lu/^{177}Hf)_{DM} = 0.0384$, $(^{176}Hf/^{177}Hf)_{DM,0} = 0.28325$ (Blichert-Toft and Albaréde, 1997; Griffin et al., 2000), ^{176}Lu decay constant $\lambda = 1.867 \times 10^{-11}$ a^{-1} (Söderlund et al., 2004).

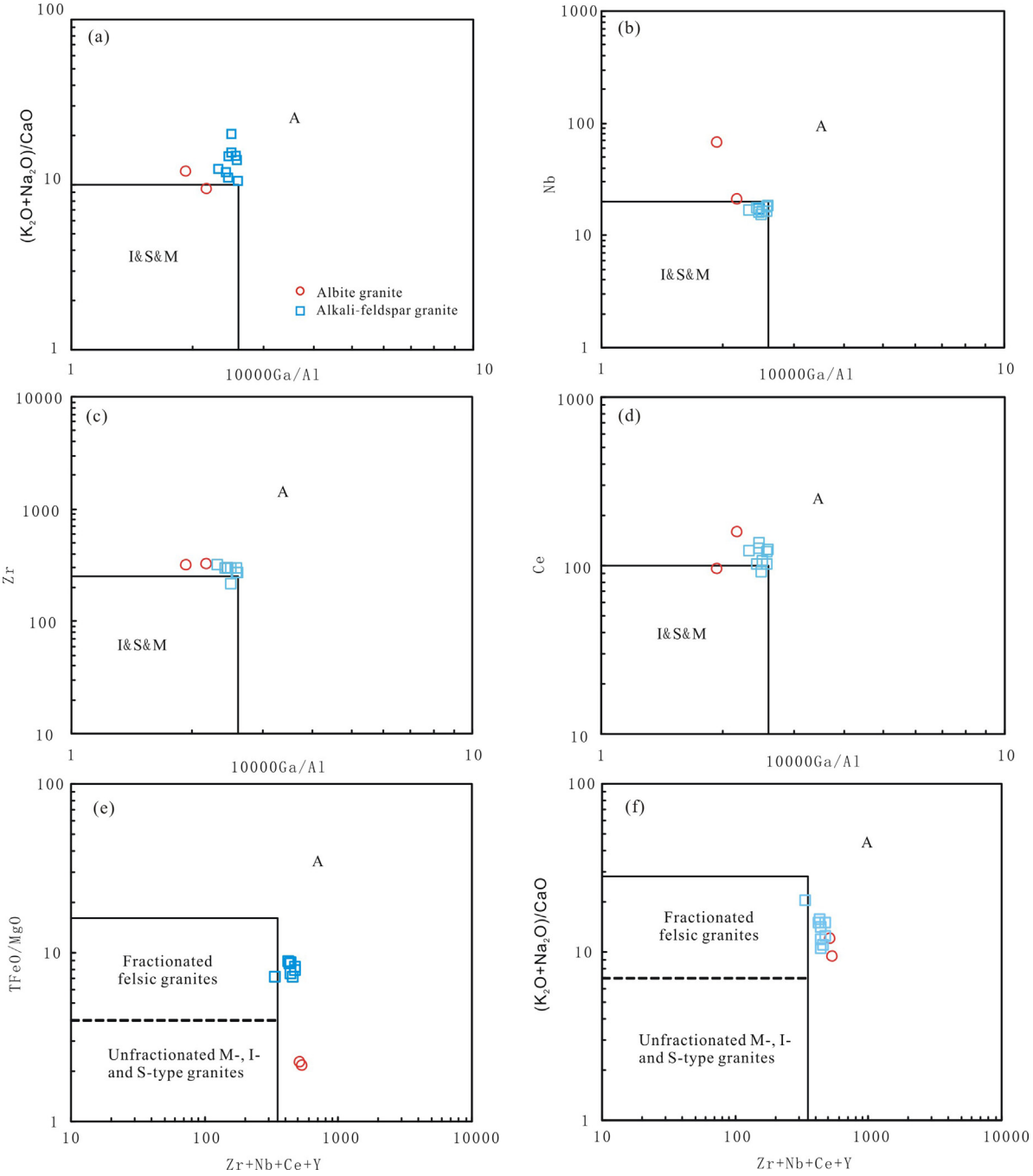

Fig. 9. Discrimination diagrams for A-type granites showing that the alkali-feldspar granite and the albite granite have A-type affinities. All the diagrams are after Whalen et al. (1987).

1993; Yang et al., 2006) and partial melting of lower crust metasomatized by mantle-derived alkali-rich fluids (e.g., Abdel-Rahman and El-Kibb, 2001; Harris et al., 1986; Martin, 2006), have also been invoked to explain the formation of A-type granites. Barboni and Bussy (2013)'s modeling showed that generation of ca. 1 km^3 highly felsic A-type granite (SiO_2 = 75.19 wt.%) through AFC process (mixing between 66 wt.% basalts and 34 wt.% Precambrian crust with 52 wt.% crystal fractionation) probably needs 11.7 km^3 crustal amphibolite for partial melting (7% melting at ca. 0.85 GPa) and basalts with thickness more than 10 km for heat supply (T = 950 °C). Although this conclusion is not always true, it at least tells that remarkably large volume of basalts are indispensable for the generation of even a small-scale felsic A-type granite produced through AFC process. Therefore, the lack of mafic rocks and mafic enclaves in this study does not favor the AFC model. In addition, assimilation of crustal materials by mantle-derived mafic melts would cause negative correlation between SiO_2 and $\varepsilon_{Nd}(t)$ and positive correlation between MgO and $\varepsilon_{Nd}(t)$, which are not recorded in the granites in this study (Fig. 12). Actually, the negative $\varepsilon_{Nd}(t)$ (<−4.4) and $\varepsilon_{Hf}(t)$ (<−3.8) values of the alkali-feldspar granite and the albite granite fall far below the depleted mantle evolutional line and are also significantly lower than those of the contemporaneous mantle-derived mafic rocks in the Jiao-Liao-Ji Belt (Fig. 13), precluding their origin from the mantle. Furthermore, these granites show ancient Nd (T_{DM2} = 2944–3051 Ma) and Hf (T_{DM2} = 2979–3179 Ma) two-stage model ages (Tables 5 and 6), which are well in accordance

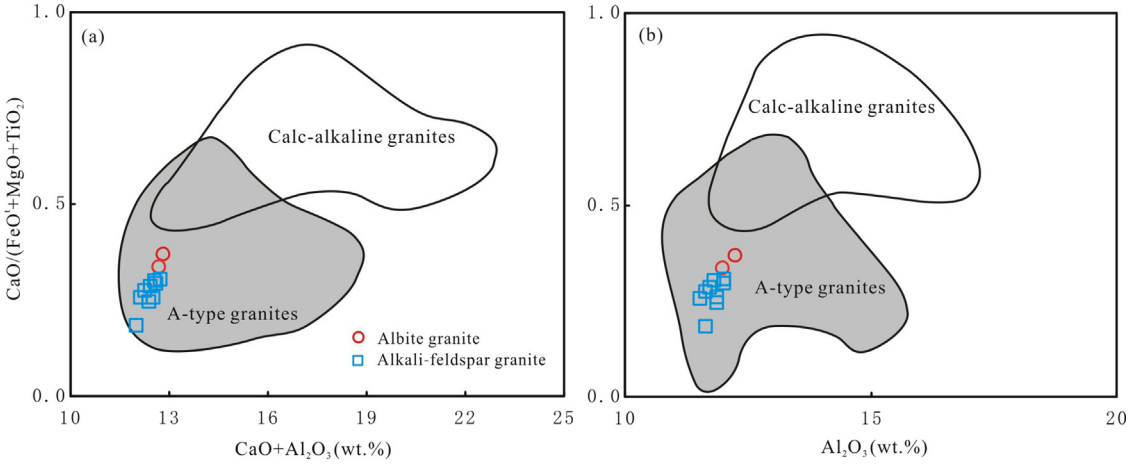

Fig. 10. Whole-rock CaO/(FeO^t + MgO + TiO$_2$) vs. (CaO + Al$_2$O$_3$) (a) and CaO/(FeO^t + MgO + TiO$_2$) vs. Al$_2$O$_3$ (b) diagrams showing the A-type affinities of the alkali-feldspar granite and the albite granite (after Dall'Agnol and de Oliveira, 2007).

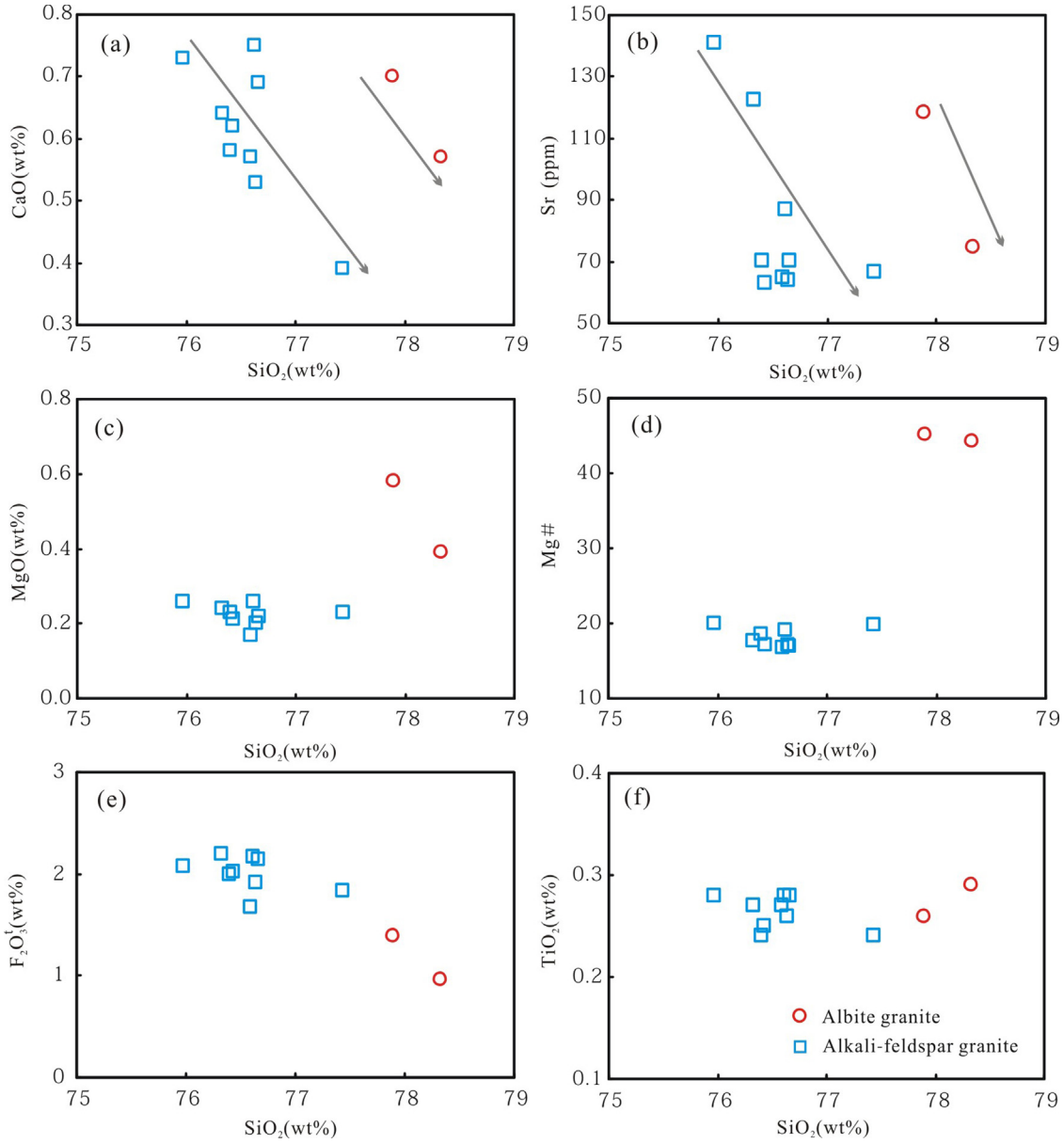

Fig. 11. Plots of CaO, Sr, MgO, Mg#, Fe$_2$O$_3^t$ and TiO$_2$ vs. SiO$_2$ for the alkali-feldspar granite and the albite granite illustrating the crystal fractionation of plagioclase (a and b) and the neglectable fractionation of mafic minerals (c–f).

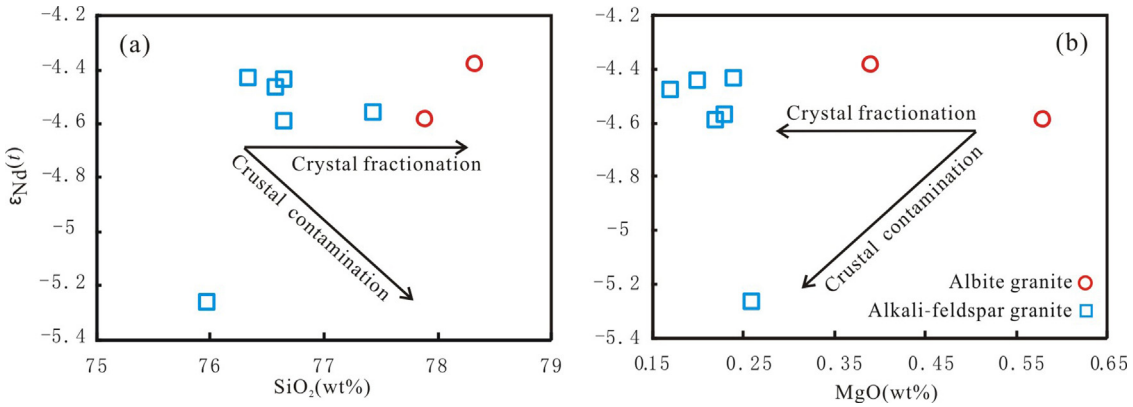

Fig. 12. Plots of SiO_2 vs. $\varepsilon_{Nd}(t)$ and MgO vs. $\varepsilon_{Nd}(t)$.

with the Mesoarchean crust evolutional trend (Fig. 13). These features, therefore, strongly suggest that the alkali-feldspar granite and the albite granite originated from the Archean crust. This conclusion is also approved by the low Nb/Ta ratios (11.8–13.9) which are similar to those of the crust-derived melts (11–12, Green, 1995).

6.3. Genetic processes of the granites

For crust-derived A-type granites, many experiments and modeling were conducted to reveal their genetic processes. Early views considered that A-type granites probably result from partial melting of F- and/or Cl-enriched, dry, granulitic residue remaining in the lower crust after extraction of an orogenic granite (e.g., Collins et al., 1982; Clemens et al., 1986; Whalen et al., 1987). However, based on mineral content and geochemistry examination on such residual source, Creaser et al. (1991) argued that the residual model could not produce the appropriate major element characteristics (such as the high $(Na_2O+K_2O)/Al_2O_3$ and TiO_2/MgO ratios) for the A-type granites and thus suggested an alternative model involving partial melting (~15–40%) of crustal igneous rocks of tonalitic to granodioritic compositions. Skjerlie and Johnston (1993) supported the above consideration by carrying out experiments on a biotite- and hornblende-bearing tonalitic gneiss at the conditions of 6 kbar and 900–975 °C as well as 10 kbar and 875–1075 °C. Furthermore, Patiño Douce (1997) also did melting experiments on calc-alkaline rocks (a tonalite and a granodiorite), demonstrating that shallow dehydration melting of hornblende- and biotite-bearing granitoids at high temperatures ($P \leq 4$ kbar, $T > 900$ °C) can generate high-silica metaluminous A-type granitic melts.

The alkali-feldspar granite and the albite granite in present study have elevated Zr concentrations (213–321 ppm) and show good development of biotite, facilitating the use of zircon saturation thermometry (T_{Zr}, Watson and Harrison, 1983) and Al^T-in-biotite geobarometer (P_{Bi}, Uchida et al., 2007) to estimate their crystallization temperatures and pressures. As a result, the T_{Zr} and P_{Bi} calculated for the alkali-feldspar granite are 823–856 °C (averaging at 839 °C) and 1.54–2.73 kbar (averaging at 2.05 kbar) respectively, while the albite granite is characterized by T_{Zr} of 851–853 °C and P_{Bi} of 2.34–2.64 kbar (averaging at 2.45 kbar) (Tables 3 and 4). In the system Qz–Ab–Or–H_2O–CO_2 at $P = 2$ kbar and $X_{H_2O} = 0.7$ projected on to the Qz–Ab–Or diagram (Holtz et al., 1992), the samples of the alkali-feldspar granite mainly plot between the 790 and 830 °C isotherms, whereas those of the albite granite plot in a separate cluster on the 870 °C isotherm (Fig. 14), conforming the above calculation. These results indicate that the initial melting P–T conditions of the source materials are probably $P < 4$ kbar and $T > 850$ °C, which are consistent with the experimental results (e.g., Patiño Douce, 1997) and also in accordance with many studies on natural samples worldwide (e.g., Barboni and Bussy, 2013; Kaur et al., 2006; King et al., 2001). Since such low pressures are comparable to the depth of upper crust and the upper crust in the study region is mainly composed of Archean meta-volcanic and meta-sedimentary rocks (such as biotite leptites, biotite-plagioclase gneisses and amphibolites) as well as TTG (tonalite–trondhjemite–granodiorite) gneisses (Jahn et al., 2008), the potential sources of the A-type granites should be the above rocks. At high temperature and low pressure conditions, melting of biotite-rich gneisses tends to generate melts extremely enriched in K_2O and depleted in Na_2O (e.g., $K_2O > 5$ wt.%, $Na_2O < 3$ wt.%, $K_2O/Na_2O > 3$) and

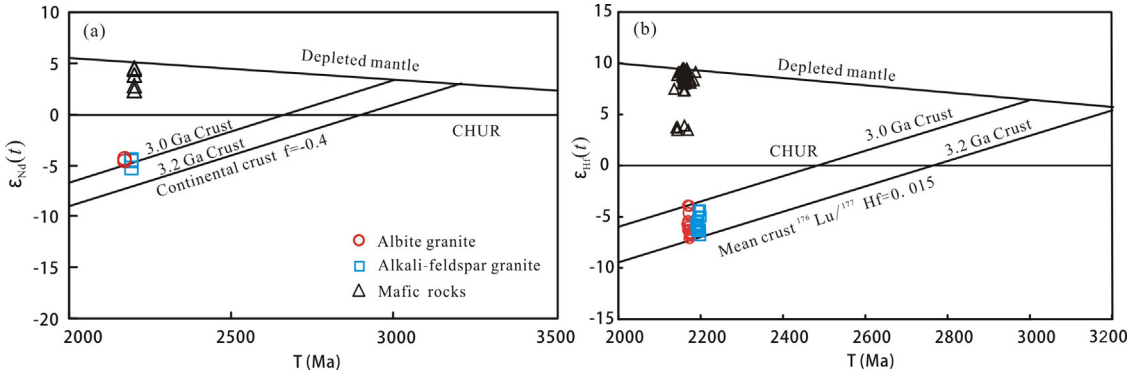

Fig. 13. Diagrams of $\varepsilon_{Nd}(t)$ and $\varepsilon_{Hf}(t)$ vs. formation ages for the alkali-feldspar granite and the albite granite. The Nd and Hf isotopic compositions of mafic rocks are from Li and Chen (2014) and Meng et al. (2014), respectively. The trend of Nd isotope evolution for the continental crust is characterized by the average "f value" (=$^{147}Sm/^{144}Nd/0.1976-1$) of −0.4 (Jahn et al., 2008) and the $^{176}Lu/^{177}Hf$ ratio of the average crust is characterized by 0.015 (Griffn et al., 2002). DM, depleted mantle evolution; CHUR, chondritic uniform reservoir evolution.

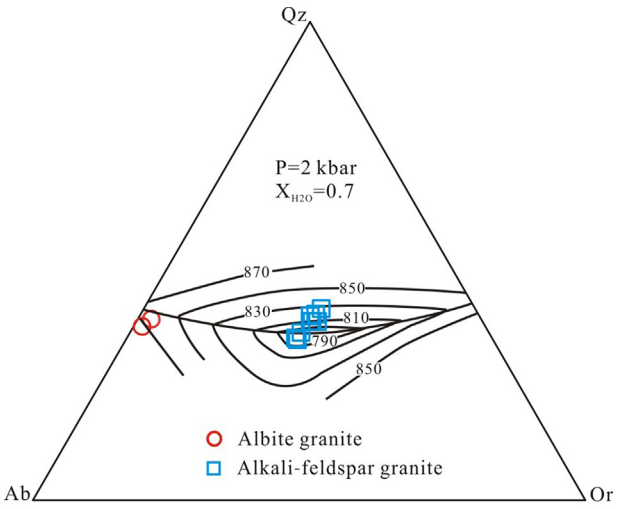

Fig. 14. The system Qz–Ab–Or–H_2O–CO_2 at 2 kbar with a fluid phase of $X_{H_2O} = 0.7$ projected on to the Qz–Ab–Or diagram (after Holtz et al., 1992).

amphibolitic rocks would like to produce granodioritic and trondhjemitic melts with high Al_2O_3 contents (commonly >13 wt.%) (e.g., Patiño Douce and Beard, 1995; Beard and Lofgren, 1991), both of which show inconsistent major element features with those of the alkali-feldspar granite and the albite granite. In addition, melting sources involving sedimentary or basaltic components commonly generate reduced A-type granites (e.g., Dall'Agnol et al., 2005; Frost and Frost, 1997; Frost et al., 1999), whereas crustal quartz-feldspathic igneous rocks likely produce oxidized ones (e.g., Dall'agnol et al., 1999; Dall'Agnol and de Oliveira, 2007). The alkali-feldspar granite shows oxidized characteristics in the $FeO^t/(FeO^t + MgO)$ vs. Al_2O_3 and $FeO^t/(FeO^t + MgO)$ vs. $Al_2O_3/(K_2O/Na_2O)$ diagrams (Fig. 15), implying that TTG gneisses rather than meta-basalts (such as amphibolites) or meta-sedimentary rocks (such as biotite leptites, biotite-plagioclase gneisses) are the favorable source materials. However, tonalitic gneisses are not favored, in that such rocks are too mafic to generate the high SiO_2 (≥76 wt.%) and low CaO (<0.8 wt.%) characteristics of the A-type granites in this study at the high temperature and low pressure conditions (e.g., Skjerlie and Johnston, 1993; Singh and Johannes, 1996; Patiño Douce, 1997). Experimental melts derived from granodiorite (SiO_2 = 69.06 wt.%) at P = 4 kbar and T = 950 °C have high SiO_2 (76.24 wt.%) and $Na_2O + K_2O$ (9.12 wt.%) and low CaO (0.62 wt.%), FeO^t (1.11 wt.%) and MgO (0.17 wt.%) compositions (Patiño Douce, 1997), resembling those of the alkali-feldspar granite (Table 4), although the experimental melts show a little lower Na_2O and higher K_2O contents (Na_2O = 2.90 wt.%, K_2O = 6.32 wt.%). The minor gaps are probably attributed to the different Na_2O and K_2O contents between the melting rocks, where the TTG gneisses in the study region are relatively enriched in Na_2O and depleted in K_2O (e.g., Jahn et al., 2008; Li et al., 2012c; Tang et al., 2007).

Notably, none of the experiments can generate the markedly low K_2O (<0.5 wt.%) and high Na_2O (>6 wt.%) characteristics of the albite granite when using tonalitic or granodioritic rocks as the melting sources, implying that the albite granite may have had unusual source rocks exceeding the above experimental rocks or have undergone uncommon magmatic processes. Considering the similar trace and rare earth elements distribution patterns, consistent Nd–Hf isotopic compositions and close spatial and temporal correlations, the albite granite should have certain genetic relationships with the alkali-feldspar granite. Crystal fractionation from the alkali-feldspar granite to the albite granite is firstly precluded. Although the alkali-feldspar granite is more mafic in SiO_2 and FeO^t contents, the much higher MgO and Mg# values of the albite granite oppose to the fractional processes, as also supported by the Harker diagrams showing no covariation between the alkali-feldspar granite and albite granite (Fig. 11). This is further confirmed by the liquidus–solidus relationships in the haplogranitic system (Holtz et al., 1992), which clearly indicate that albite granite cannot be produced by crystal fractionation of granitic magma alone (Azer et al., 2010; Chaudhri et al., 2003). Actually, several literatures have reported the comagmatic associations of A-type alkali-feldspar granites and albite granites (e.g., Azer et al., 2010; Barboni and Bussy, 2013; Chaudhri et al., 2003; Kaur et al., 2006, 2007, 2011), which proposed genetic models for albite granites at least including: (1) albite metasomatism on original alkali-feldspar granite as a consequence of pervasive infiltration of a high Na/(Na + K) fluid at the late-magmatic stage (e.g., Kaur et al., 2006); (2) Na-rich residual melt extracted from partially crystallized A-type granite magmas or melting of plagioclase-rich layers formed during A-type granite differentiation (e.g., Azer et al., 2010; Barboni and Bussy, 2013). Albitization of plagioclase commonly leads to the formation of pectolite and results in serious loss of most trace elements and REEs besides major elements of CaO, Al_2O_3, K_2O and FeO (Hövelmann et al., 2010). However, pectolite is not observed in the albite granite and the albite granite shows similar REE contents (even higher HREE contents, Fig. 8b) to those of the alkali-feldspar granite. In addition, the chemical index of alteration (CIA) in the

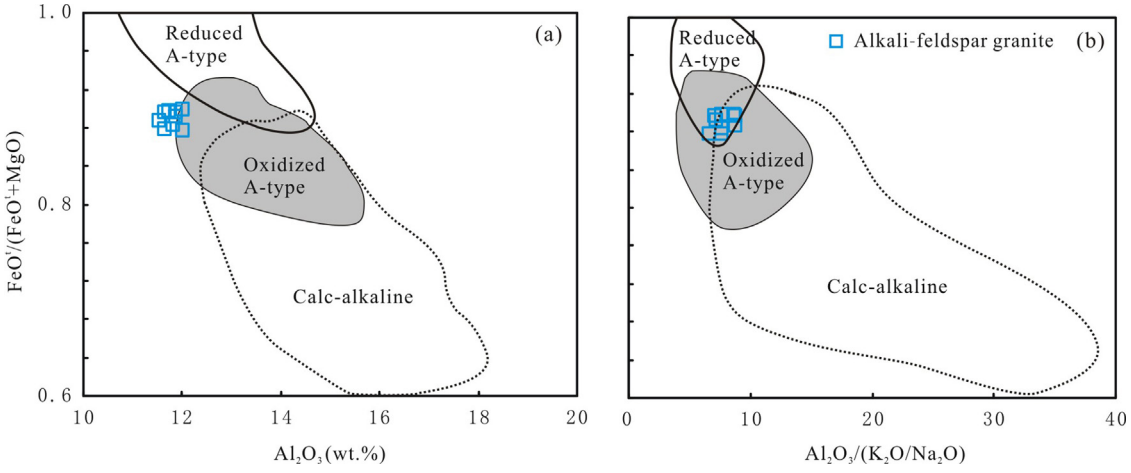

Fig. 15. $FeO^t/(FeO^t + MgO)$ vs. Al_2O_3 (a) and $FeO^t/(FeO^t + MgO)$ vs. $Al_2O_3/(K_2O/Na_2O)$ (b) diagrams showing the oxidized features of the alkali-feldspar granite (after Dall'Agnol and de Oliveira, 2007). The albite granite falls out of the fields due to its unusual low FeO^t content and extremely high $Al_2O_3/(K_2O/Na_2O)$ ratio.

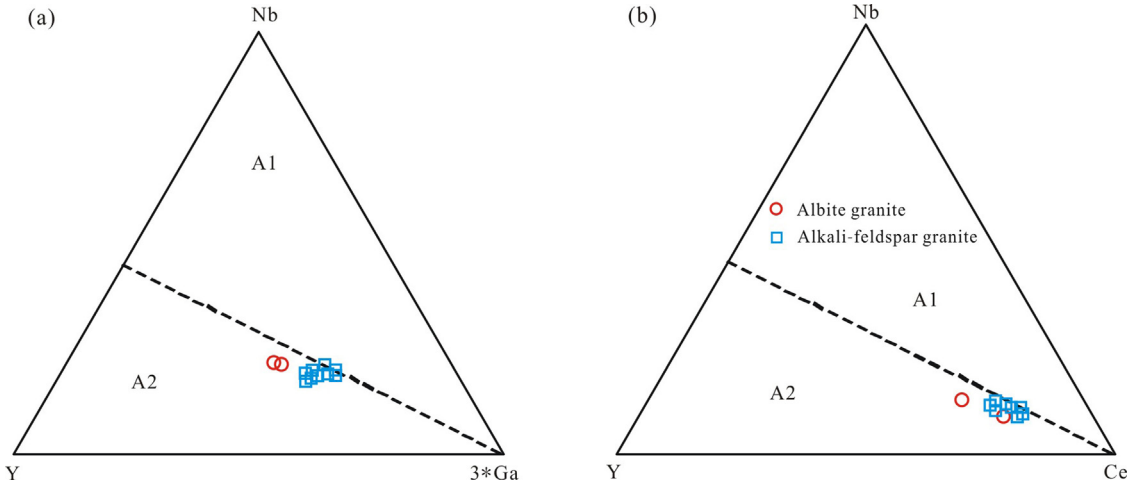

Fig. 16. Triangular plots of Nb–Y–3Ga (a) and Nb–Y–Ce (b) for distinguishing between A1 and A2 granitoids (after Eby, 1992).

albite granite varies between 50.2 and 50.3 (Table 4), within the range of fresh granites (45–55, Nesbitt and Young, 1982). Most importantly, coexistent biotite and albite grains as well as euhedral zircon inclusions in albite crystals have been identified from the albite granite (Fig. 3g and h), which suggest the magmatic origin of the albite. In conclusion, the intrusive contacts between the albite granite and the wallrocks (Fig. 3a and b), the lack of albitization overprinted on the alkali-feldspar granite (Fig. 3c and d) and the magmatic texture of the albite granite (Fig. 3e–f) approve a magmatic instead of a metasomatic origin for the albite granite. Cooling of a large pluton (such as 10 km wide and 15 km high) within upper crust only requires tens of thousands of years to a few million years (e.g., Cathles et al., 1997; Lake, 2013; Sano et al., 2002) The large age gap between the alkali-feldspar granite and the albite granite (>20 Ma, Fig. 5) suggests that the alkali-feldspar might have been completely solidified when the albite granite was emplaced, and therefore extraction of Na-rich residual melt from partially crystallized A-type granite magmas is also excluded. Finally, partial melting of plagioclase-rich layers is hoped to produce the albite granite. Experiments showed that plagioclase (mainly andesine, An_{30-50}) and orthopyroxene are the dominant crystallization phases in the A-type melts derived from melting of tonalitic and granodioritic rocks at T = 850–950 °C and P = 2–6 kbar (e.g., Patiño Douce, 1997; Klimm et al., 2003; Skjerlie and Johnston, 1993). Accumulation of such crystallizing minerals is expected to form plagioclase-rich layers. Since orthopyroxene is stable up to much higher temperatures (e.g., Nair and Chacko, 2002; Skjerlie and Johnston, 1993), the melting behaviors of the plagioclase-rich layers can be estimated using the Ab–An ± Qz–H_2O systems drawn from experiments by Johannes (1978, 1989) and Johannes and Holtz (1989) at P_{H_2O} = 2–5 kbar. In these systems, melting of plagioclases with An_{30-50} can generate sodic melts with An_{2-12} at the temperatures ranging from 700 °C to 820 °C. The melts show An features well consistent with those of the albite granite. However, the low temperatures required for plagioclase melting do not agree with the high temperatures inferred for the albite granite. If the Ab–An system is in absence of SiO_2 and H_2O, the melting temperatures of the plagioclases (An_{30-50}) will be elevated to be as high as 1175–1180 °C to produce Na-rich melts (An_{2-12}) (e.g., Bowen, 1913). It tells that the generation of Na-rich melts at high temperature and low pressure conditions can be realized in the presence of appropriate SiO_2 and H_2O contents. If it is true, the origin of the albite granites from partial melting of the plagioclase-rich layers formed after the extraction of the alkali-feldspar granite seems applicable. This model can well explain the similar geochemical compositions between the albite granite and the alkali-feldspar granite and the significant higher MgO and Mg# values as well as the smaller scale of the albite granite.

Other Na-rich rocks such as trondhjemitic gneisses are also widely distributed in the study region (e.g., Jahn et al., 2008; Li et al., 2012c; Tang et al., 2007), which may contribute to the generation of the albite granite. However, the trondhjemitic gneisses contain K_2O contents commonly higher than 2 wt.% (e.g., Jahn et al., 2008; Li et al., 2012c; Tang et al., 2007), partial melting of which would not generate the low K_2O features of the albite granite (K_2O < 0.5 wt.%). Most importantly, melting of trondhjemitic gneisses is hard to explain the elevated MgO (0.39–0.58 wt.%) and Mg# (44.3–45.2) values of the albite granite, which are remarkably higher than those of the alkali-feldspar granite (MgO = 0.17–0.26 wt.%, Mg# = 16.8–19.9) derived from the granodioritic rocks. It is noteworthy that the presence of inherited zircons showing age variation of 2192–2243 Ma in the albite granite probably indicates minor contamination from wallrocks during magma emplacement.

6.4. Tectonic implications

As one of the most famous types of granitoids, A-type granites are commonly considered to be produced in extensional settings related to hotspots, plumes, continental rifts and post-collision (Eby, 1992; Whalen et al., 1987). Eby (1992) correlated the A-type granites to their tectonic settings by using the A1-A2 diagrams, which classified the A-type granites into A1 and A2 groups and suggested that the A1 group represents differentiates of magmas derived from sources like those of oceanic-island basalts but emplaced in continental rifts or during intra-plate magmatism, whereas the A2 group represents magmas derived from continental crust or underplated crust that has been through a cycle of continent-continent collision or island-arc magmatism. The samples of the alkali-feldspar granite and the albite granite mainly fall into the A2 field in the A1–A2 discrimination diagrams (Fig. 16), well consistent with their crustal origin. However, it should be noted that the A1 and A2 discriminant diagrams can only be used for granitoids that plot both in the within-plate granite field of Pearce et al. (1984) and the A-type granitoid field of the Ga/Al plots of Whalen et al. (1987), as emphasized by Eby (1992). Unfortunately, most samples of our granites do not fall into the within-plate granite field of Pearce et al. (1984) (Fig. 17), indicating that using the A1–A2 diagrams to identify the tectonic setting of the granites may not be reliable. Therefore, other evidence should be invoked to

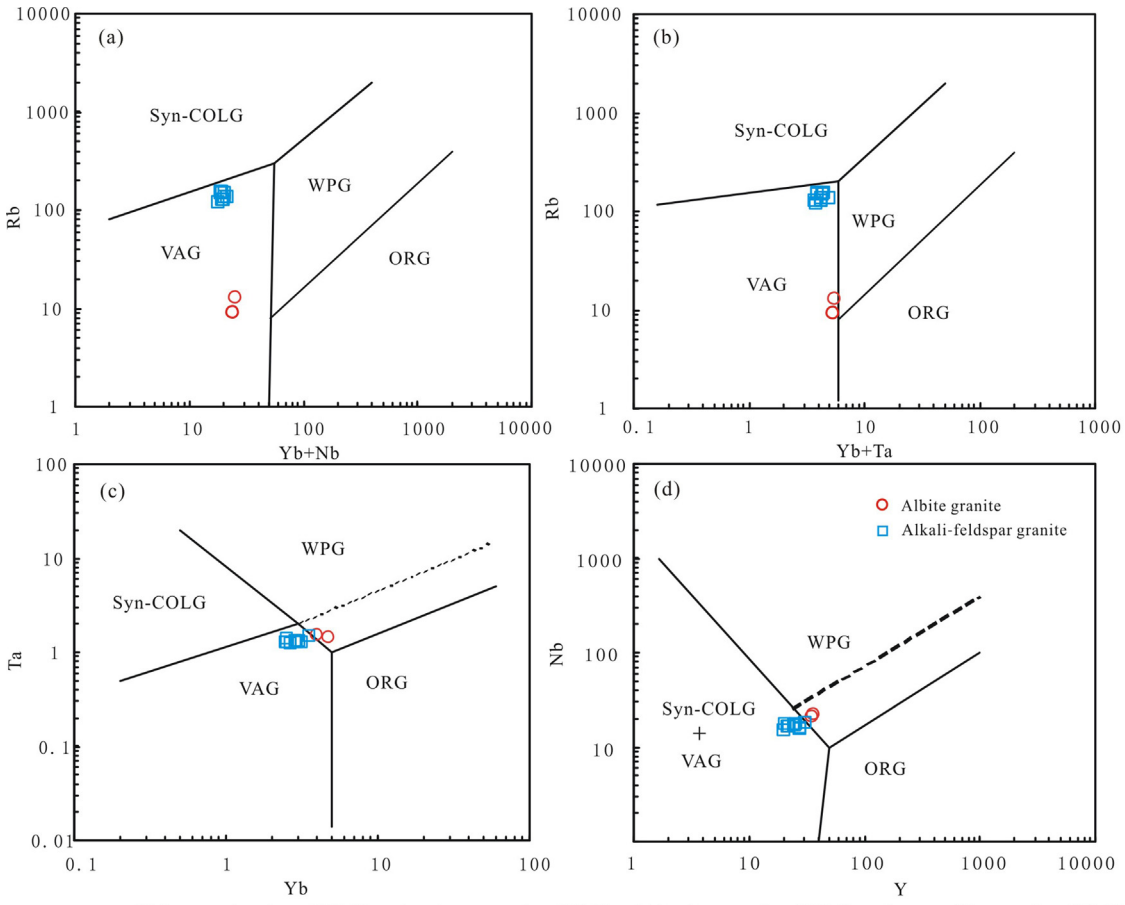

Fig. 17. Rb vs. (Yb + Nb) (a), Rb vs. (Yb + Ta) (b), Ta vs. Yb (c) and Nb vs. Y (d) discrimination diagrams for syn-collision granites (syn-COLG), volcanic arc granites (VAG), within plate granites (WPG) and ocean ridge granites (ORG). All the diagrams are after Pearce et al. (1984).

illustrate the tectonic setting. The unusual association of alkali-feldspar granite and albite granite has been commonly found in continental rifts (e.g., Barboni and Bussy, 2013; Chaudhri et al., 2003; El Dabe, 2013; Kaur et al., 2006, 2011), which likely indicates a continental rift for the granites in this study. Based on *P–T* calculations, the emplacement depth from the alkali-feldspar granite to the albite granite becomes shallower as the crystallization temperature increases. This fact may imply a continuous crustal extension under high heat flow during 2171–2193 Ma. Such continuous extension coupled with extraordinarily high temperature matches well with rifting process. The protoliths of the Paleoproterozoic amphibolites widely distributed as the wallrocks of the granites show affinities to continental tholeiites, which also suggest an intra-plate setting instead of a subduction environment (Lan et al., 2014a). Actually, bimodal volcanic rocks (Peng and Palmer, 1995; Sun et al., 1996; Yu, 1996; Zhang and Yang, 1988) and non-marine borate deposits (Hu et al., 2015; Jiang et al., 1997; Peng and Palmer, 1995, 2002) have long been identified in the volcanic-sedimentary successions of the Jiao-Liao-Ji Belt, both of which favor a continental rift. Therefore, we consider that the A-type granites in this study indicate continental rifting during 2.1–2.2 Ga.

However, it should also be noted that sediments and meta-mafic rocks characterized by active continental margin/magmatic arc signatures were recognized in the northern segment of the Jiao-Liao-Ji Belt in recent years (e.g., Li and Chen, 2014; Meng et al., 2013, 2014). In addition, more and more evidence show that both the Fenzishan (e.g., Li et al., 2003; Lu, 1996) and Jingshan (e.g., Tam et al., 2011, 2012a,b,c; Wang et al., 2010; Zhou et al., 2007) groups in the southern segment of the Jiao-Liao-Ji Belt likely suffered clockwise P-T path. These observations contradict the rift model. An alternative way to explain such contradiction may be that the rift once developed into an incipient ocean and finally was closed upon itself through subduction and collision (Tam et al., 2012a,b,c; Zhao and Zhai, 2013). Actually, some significant but commonly ignored phenomenons indeed support the rift evolving from the southern to the northern segments of the Jiao-Liao-Ji Belt: (1) The southern segment was deposited at some time earlier than the northern segment. The youngest group of detrital zircons obtained from the Fenzishan and Jingshan groups in the southern segment mainly concentrates at the ages of 2.2–2.3 Ga (Lan et al., 2014a; Wan et al., 2006), which are obvious older than those in the North and South Liaohe groups from the northern segment (2.0–2.2 Ga, Luo et al., 2004, 2008; Wan et al., 2006); (2) The emplacement of the A-type granites postdated the deposition of the Paleoproterozoic successions in the southern segment, whereas in the northern segment such granites (e.g., the Liaoji granites, 2166–2176 Ma) were emplaced before the deposition of the Paleoproterozoic sequences (Li and Zhao, 2007; Lu et al., 2004, 2006). These facts at least indicate that the opening process of the rift was never stopped during 2.0–2.2 Ga throughout the Jiao-Liao-Ji Belt. Such a long-term opening certainly has the potential to form an incipient ocean. However, the evidence presented in this study are far from enough to confirm the transformation from a rift to an ocean, and thus further studies on the evolutionary histories of the Paleoproterozoic successions are required. The emplacement of the A-type granites in this study can constrain that the southern segment of the Jiao-Liao-Ji Belt experienced continental rifting at its early stage (~2.2 Ga).

Contemporaneous A-type granites (2.1–2.2 Ga) were widely found in the Paleoproterozoic belts of the NCC, such as in the Liao-Ji (e.g., Han and Xia, 2009; Li et al., 2005; Li and Yang, 1997; Li and Zhao, 2007; Lu et al., 2004, 2006), Jiaobei Terrane (e.g., Liu et al., 2014) and Bengbu (e.g., Yang et al., 2009) areas of the Jiao-Liao-Ji Belt, and in the Lüliang (e.g., Du et al., 2012), Wutai (e.g., Du et al., 2013), Zanhuang (e.g., Yang et al., 2011) and Lushan (e.g., Zhou et al., 2014) areas of the Trans-North China Orogen, almost all of which were considered to be derived from reworking of the Archean to Paleoproterozoic crust in extensional settings. However, their tectonic environments remain hotly debated. Distinct environments of continental rift (e.g., Du et al., 2013; Li et al., 2005; Li and Zhao, 2007; Peng et al., 2012; Zhou et al., 2014) and magmatic arc (e.g., Du et al., 2012; Lu et al., 2006; Zhao et al., 2008) have been proposed for them. Integrated consideration on these granites may be helpful to reveal their tectonic backgrounds. Considering these A-type granites showing great simultaneity and mostly originating from partial melting of the Archean crust, regional intense extension of the basements of the NCC probably occurred during 2.1–2.2 Ga, which therefore imply that rifting of a coherent craton likely operated during Paleoproterozoic.

7. Conclusions

Comprehensive geochronological, mineralogical, geochemical and isotopic investigations on the Paleoproterozoic granites from the Changyi area of the Jiao-Liao-Ji Belt lead to the following conclusions.

(1) The Paleoproterozoic granites can be divided into alkali-feldspar granite and albite granite, both of which belong to A-type granite and were emplaced during 2171–2193 Ma.
(2) These granites were derived from partial melting of the Archean crust at high temperature and low pressure conditions (probably $T > 850\,^{\circ}C$, and $P < 4$ kbar). However, the source materials of the granites show some difference. The alkali-feldspar granite was likely sourced from melting of the granodioritic rocks, whereas the albite granite probably originated from reworking of the plagioclase-rich layers after extraction of the A-type melts.
(3) The unusual association of A-type alkali-feldspar granite and albite granite strongly suggests continental rifting during Paleoproterozoic in the Jiao-Liao-Ji Belt of the eastern NCC.

Acknowledgements

We are grateful to Chao-Feng Li and Qian-Nan Li for help during Sr–Nd isotopes analyses, Yong-ShengLiu for help during LA–ICP-MS zircon U–Pb dating, Yue-Heng Yang for help during zircon Hf analyses, Xiang-Kun Ge for help during Electron microprobe analyses, and He Li and Wen-Jun Li for help during major and trace elements analyses. This study was financially supported by the Natural Science Foundation of China (41202065), the Major State Basic Research Development Program (2012CB416605) and the Youth Innovation Promotion Association, Chinese Academy of Sciences.

References

Abdel-Rahman, A.M., El-Kibb, M.M., 2001. Anorogenic magmatism: chemical evolution of the Mount El-Sibai A-type complex (Egypt), and implications for the origin of within-plate felsic magmas. Geol. Mag. 158, 67–85.
Anderson, I.C., Frost, C.D., Frost, B.R., 2003. Petrogenesis of the Red Mountain pluton, Laramie anorthosite complex, Wyoming: implications for the origin of A-type granite. Precambrian Res. 124, 243–267.
Azer, M.K., Stern, R.J., Kimura, J.I., 2010. Origin of a late Neoproterozoic (605 ± 13 Ma) intrusive carbonate–albitite complex in Southern Sinai, Egypt. Int. J. Earth Sci. 99, 245–267.
Barboni, M., Bussy, F., 2013. Petrogenesis of magmatic albite granites associated to cogenetic A-type granites: Na-rich residual melt extraction from a partially crystallized A-type granite mush. Lithos 177, 328–351.
Barker, F., 1979. Trondhjemite: definition, environment and hypothesis of origin. In: Barker, F. (Ed.), Trondhjemites, Dacites and Related Rocks. Elsevier, Amsterdam, pp. 1–12.
Beard, J.S., Lofgren, G.E., 1991. Dehydration melting and water-saturated melting of basaltic and andesitic greenstones and amphibolites at 1, 3 and 6.9 kb. J. Petrol. 32, 365–401.
Bédard, J., 1990. Enclaves from the A-type granite of the Mégantic Complex, White Mountain Magma Series: clues to granite magmagenesis. J. Geophys. Res.: Solid Earth 95, 17797–17819.
Blichert-Toft, J., Albaréde, F., 1997. The Lu–Hf isotope geochemistry of chondrites and the evolution of the mantle–crust system. Earth Planet. Sci. Lett. 148, 243–258.
Bonin, B., 2007. A-type granites and related rocks: evolution of a concept, problems and prospects. Lithos 97, 1–29.
Bowen, N.L., 1913. The melting phenomena of the plagioclase feldspars. Am. J. Sci. 35, 577–599.
Cathles, L.M., Erendi, A.H.J., Barrie, T., 1997. How long can a hydrothermal system be sustained by a single intrusive event? Econ. Geol. 92, 766–771.
Chappell, B.W., White, A.J.R., 1974. Two contrasting granite types. Pacific Geol. 8, 173–174.
Chappell, B.W., White, A.J.R., 2001. Two contrasting granite types: 25 years later. Aust. J. Earth Sci. 48, 489–499.
Chaudhri, N., Kaur, P., Okrusch, M., Schimrosczyk, A., 2003. Characterisation of the Dabla granitoids, North Khetri Copper Belt, Rajasthan, India: evidence of bimodal anorogenic felsic magmatism. Gondwana Res. 6, 879–895.
Chen, S.L., Huan, Y.Q., Bing, Z.B., 2001. Characteristics of Palaeoproterozoic intrusive rocks and continental dynamic evolution of tectono-magmatism in the eastern Liaoning. Liaoning Geol. 18, 43–50 (in Chinese with English Abstract).
Clarke, D.B., 1992. Granitoid Rocks. Topics in the Earth Sciences. Chapman and Hall, London, 283pp.
Clemens, J.D., Holloway, J.R., White, A.J.R., 1986. Origin of an A-type granite: experimental constraints. Am. Mineral. 71, 317–324.
Collins, W.J., Beams, S.D., White, A.J.R., Chappell, B.W., 1982. Nature and origin of A-type granites with particular reference to southeastern Australia. Contrib. Mineral. Petrol. 80, 189–200.
Creaser, R.A., Price, R.C., Wormald, R.J., 1991. A-type granites revisited: assessment of a residual-source model. Geology 19, 163–166.
Dall'Agnol, R., de Oliveira, D.C., 2007. Oxidized, magnetite-series, rapakivi-type granites of Carajás, Brazil: implications for classification and petrogenesis of A-type granites. Lithos 93, 215–233.
Dall'agnol, R., Scaillet, B., Pichavant, M., 1999. An experimental study of a lower Proterozoic A-type granite from the Eastern Amazonian Craton, Brazil. J. Petrol. 40, 1673–1698.
Dall'Agnol, R., Teixeira, N.P., Rämö, O.T., Moura, C.A.V., Macambira, M.J.B., Oliveira, D.C., 2005. Petrogenesis of the Paleoproterozoic, rapakivi, A-type granites of the Archean Carajás Metallogenic Province, Brazil. Lithos 80, 101–129.
De la Roche, H., Leterrier, J., Granclaude, P., Marchal, M., 1980. A classification of volcanic and plutonic rocks using R1–R2 diagram and major-element analyses – its relationships with current nomenclature. Chem. Geol. 29, 183–210.
Dong, Y.S., Wang, W., 1998. The style of metamorphic evolution of early Proterozoic Jingshan Group in Eastern Shandong Province and its tectonic environment. Glob. Geol. 17, 1–8 (in Chinese with English abstract).
Du, L.L., Yang, C.H., Ren, L.D., Song, H.X., Geng, Y.S., Wan, Y.S., 2012. The 2.2–2.1 Ga magmatic event and its tectonic implication in the Lüliang Mountains, North China Craton. Acta Petrol. Sinica 28, 2751–2769 (in Chinese with English abstract).
Du, L.L., Yang, C.H., Wang, W., Ren, L.D., Wan, Y.S., Wu, J.S., Zhao, L., Song, H.X., Geng, Y.S., Hou, K.J., 2013. Paleoproterozoic rifting of the North China Craton: geochemical and zircon Hf isotopic evidence from the 2137 Ma Huangjinshan A-type granite porphyry in the Wutai area. J. Asian Earth Sci. 72, 190–202.
Eby, G.N., 1990. The A-type granitoids: a review of their occurrence and chemical characteristics and speculations on their petrogenesis. Lithos 26, 115–134.
Eby, G.N., 1992. Chemical subdivision of the A-type granitoids; petrogenetic and tectonic implications. Geology 20, 641–644.
Faure, M., Trap, P., Lin, W., Monie, P., Bruguier, O., 2007. Polyorogenic evolution of the Paleoproterozoic Trans-North China Belt – new insights from the Lüliangshan–Hengshan–Wutaishan and Fuping massifs. Episodes 30, 95–106.
El Dabe, M.M., 2013. A geochemical tectonomagmatic classification of the A-type granitoids based on their magma types and tectonic regimes. Arab. J. Geosci. 8, 187–193.
Faure, M., Lin, W., Moni, P., Bruguier, O., 2004. Paleoproterozoic arc magmatism and collision in Liaodong Peninsula, NE China. Terra Nova 16, 75–80.
Frost, B.R., Barnes, C.G., Collins, W.J., Arculus, R.J., Ellis, D.J., Frost, C.G., 2001. A geochemical classification for granitic rocks. J. Petrol. 42, 2033–2048.
Frost, C.D., Frost, B.R., 1997. Reduced rapakivi type granites: the tholeiitic connection. Geology 25, 647–650.
Frost, C.D., Frost, B.R., Chamberlain, K.R., Edwards, B., 1999. Petrogenesis of the 1.43 Ga Sherman batholith, SE, Wyoming, USA: a reduced, rapakivi-type anorogenic granite. J. Petrol. 40, 1771–1802.
Gao, S., Zhang, J.F., Xu, W.L., Liu, Y.S., 2009. Delamination and destruction of the North China Craton. Chin. Sci. Bull. 54, 3367–3378.
Glikson, A.Y., 1979. Early Precambrian tonalite-trondhjemite sialic nuclei. Earth-Sci. Rev. 15, 1–73.

Green, T.H., 1995. Significance of Nb/Ta as an indicator of geochemical processes in the crust–mantle system. Chem. Geol. 120, 347–359.
Griffin, W.L., Pearson, N.J., Belousova, E., Jackson, S.E., Achterbergh, E.V., O'Reilly, S.Y., Shee, S.R., 2000. The Hf isotope composition of cratonic mantle: LAM–MC–ICPMS analysis of zircon megacrysts in kimberlites. Geochim. Cosmochim. Acta 64, 133–147.
Griffin, W.L., Pearson, N.J., Belousova, E.A., Saeed, A., 2006. Comment: Hf-isotope heterogeneity in zircon 91500. Chem. Geol. 233, 358–363.
Griffin, W.L., Wang, X., Jackson, S.E., Pearson, S.E., O'Reilly, S.Y., Xu, X.S., Zhou, X.M., 2002. Zircon chemistry and magma mixing, SE China: in-situ analysis of Hf isotopes, Tonglu and Pingtan igneous complexes. Lithos 61, 237–269.
Haapala, I., Frindt, S., Kandara, J., 2007. Cretaceous Gross Spitzkoppe and Klein Spitzkoppe stocks in Namibia: topaz-bearing A-type granites related to continental rifting and mantle plume. Lithos 97, 174–192.
Han, J., Xia, Y.L., 2009. Discussion on zircon LA–ICP-MS ages of Lianshanguan-Gaojiagou granites and its significance. Uranium Geol. 25, 214–221 (in Chinese with English abstract).
Hao, D.F., Li, S.Z., Zhao, G.C., Sun, M., Han, Z.Z., Zhao, G.T., 2004. Origin and its constraint to tectonic evolution of Paleoproterozoic granitoids in the eastern Liaoning and Jilin province, North China. Acta Petrol. Sinica 20, 1409–1416 (in Chinese with English abstract).
Harris, N.B.W., Marzouki, F.M.H., Ali, S., 1986. The Jabel Sayid complex, Arabian Shield: geochemical constraints on the origin of peralkaline and related granites. J. Geol. Soc. Lond. 143, 287–295.
He, G.P., Ye, H.W., 1998. Two type of Early Proterozoic metamorphism in the eastern Liaoning to southern Jilin and their tectonic implication. Acta Petrol. Sinica 14, 152–162 (in Chinese with English abstract).
Hofmann, A.W., 1997. Mantle geochemistry, the message from oceanic volcanism. Nature 385, 219–229.
Holtz, F., Pichavant, M., Barbey, P., Johannes, W., 1992. Effects of H_2O on liquidus phase relations in the haplogranite system at 2 and 5 kbar. Am. Mineral. 77, 1233–1241.
Hövelmann, J., Putnis, A., Geisler, T., Schmidt, B.C., Golla-Schindler, U., 2010. The replacement of plagioclase feldspars by albite: observations from hydrothermal experiments. Contrib. Mineral. Petrol 159, 43–59.
Hu, G., Li, Y., Fan, C., Hou, K., Zhao, Y., Zeng, L., 2015. In situ LA–MC–ICP-MS boron isotope and zircon U–Pb age determinations of Paleoproterozoic borate deposits in Liaoning Province, northeastern China. Ore Geol. Rev. 65, 1127–1141.
Jahn, B.M., Liu, D.Y., Wan, Y.S., Song, B., Wu, J.S., 2008. Archean crustal evolution of the Jiaodong peninsula, China, as revealed by zircon SHRIMP geochronology, elemental and Nd-isotope geochemistry. Am. J. Sci. 308, 232–269.
Jiang, S.Y., Palmer, M.R., Peng, Q.M., Yang, J.H., 1997. Chemical and stable isotopic compositions of Proterozoic metamorphosed evaporites and associated tourmalines from the Houxianyu borate deposit, eastern Liaoning, China. Chem. Geol. 135, 189–211.
Johannes, W., 1978. Melting of plagioclase in the system Ab–An–H_2O and Qz–Ab–An–H_2O at P_{H2O} = 5 kbar, an equilibrium problem. Contrib. Mineral. Petrol. 66, 295–303.
Johannes, W., 1989. Melting of plagioclase–quartz assemblages at 2 kbar water pressure. Contrib. Mineral. Petrol. 103, 270–276.
Johannes, W., Holtz, F., 1989. Melting of plagioclase in granite and related systems: composition of coexisting phases and kinetic observations. Trans. R. Soc. Edinb.: Earth Sci. 83, 417–422.
Kaur, P., Chaudhri, N., Raczek, I., Kröner, A., Hofmann, A.W., 2007. Geochemistry, zircon ages and whole-rock Nd isotopic systematics for Palaeoproterozoic A-type granitoids in the northern part of the Delhi belt, Rajasthan, NW India: implications for late Palaeoproterozoic crustal evolution of the Aravalli craton. Geol. Mag. 144, 361–378.
Kaur, P., Chaudrih, N., Okrush, M., Koepke, J., 2006. Palaeoproterozoic A-type felsic magmatism in the Khetri Copper Belt, Rajasthan, northwestern India: petrologic and tectonic implications. Mineral. Petrol. 87, 81–122.
Kaur, P., Chaudhri, N., Raczek, I., Kröner, A., Hofmann, A.W., Okrusch, M., 2011. Zircon ages of late Palaeoproterozoic (ca. 1.72–1.70 Ga) extension-related granitoids in NE Rajasthan, India: regional and tectonic significance. Gondwana Res. 19, 1040–1053.
Kerr, A., Fryer, B.J., 1993. Nd isotopic evidence for crust–mantle interaction in the generation of A-type granitoid suites in Labrador, Canada. Chem. Geol. 104, 39–60.
King, P.L., Chappell, B.W., Allen, C.M., White, A.J.R., 2001. Are A-type granites the high temperature felsic granites? Evidence from fractionated granites of the Wangrah Suite. Aust. J. Earth Sci. 48, 501–514.
Klimm, K., Holtz, F., Johannes, W., King, P.L., 2003. Fractionation of metaluminous A-type granites: an experimental study of the Wangrah Suite, Lachlan Fold Belt, Australia. Precambrian Res. 124, 327–341.
Kusky, T.M., 2011. Geophysical and geological tests of tectonic models of the North China Craton. Gondwana Res. 20, 26–35.
Lake, E.T., 2013. Crystallization and saturation front propagation in silicic magma chambers. Earth Planet. Sci. Lett. 383, 182–193.
Lan, T.G., Fan, H.R., Hu, F.F., Yang, K.F., Cai, Y.C., Liu, Y.S., 2014a. Depositional environment and tectonic implications of Paleoproterozoic BIF in the Changyi area, eastern North China Craton: evidence from geochronology and geochemistry of wallrocks. Ore Geol. Rev. 61, 52–72.
Lan, T.G., Fan, H.R., Santosh, M., Hu, F.F., Yang, K.F., Yang, Y.H., Liu, Y.S., 2014b. U–Pb zircon chronology, geochemistry and isotopes of the Changyi banded iron formation in eastern Shandong Province: constraints on BIF genesis and implications for Paleoproterozoic tectonic evolution of the North China Craton. Ore Geol. Rev. 56, 472–486.
Landenberger, B., Collins, W.J., 1996. Derivation of A-type granites from a dehydrated Charnockitic lower crust: evidence from the Chaelundi Complex, Eastern Australia. J. Petrol. 37, 145–170.
Li, C.F., Li, X.H., Li, Q.L., Guo, J.H., Li, X.H., Yang, Y.H., 2012a. Rapid and precise determination of Sr and Nd isotopic ratios in geological samples from the same filament loading by thermal ionization mass spectrometry employing a single-step separation scheme. Anal. Chim. Acta 727, 54–60.
Li, C.F., Li, X.H., Li, Q.L., Guo, J.H., Li, X.H., Feng, L.J., Chu, Z.Y., 2012b. Simultaneous determination of $^{143}Nd/^{144}Nd$ and $^{147}Sm/^{144}Nd$ ratios and Sm–Nd contents from the same filament loaded with purified Sm–Nd aliquot from geological samples by isotope dilution thermal ionization mass spectrometry. Anal. Chem. 84, 6040–6047.
Li, H.K., Geng, K., Zhuo, C.Y., Liang, D.T., Chen, L., 2012c. Evolution and continental crust growth of early Precambrian granitoids in eastern Shandong Province. Shandong Land Resour. 28, 8–14 (in Chinese with English abstract).
Li, S., Zhao, G., Sun, M., Han, Z., Luo, Y., Hao, D., Xia, X., 2005. Deformation history of the Paleoproterozoic Liaohe assemblage in the Eastern Block of the North China Craton. J. Asian Earth Sci. 24, 659–674.
Li, S.Z., Han, Z.Z., Liu, Y.J., Yang, Z.S., Ma, R., 2001. Continental dynamics and regional metamorphism in the Liaohe Group. Geol. Rev. 47, 9–18 (in Chinese with English abstract).
Li, S.Z., Hao, D.F., Han, Z.Z., Zhao, G.C., Sun, M., 2003. Paleoproterozoic deep processes and tectono-thermal evolution in Jiao-Liao Massif. Acta Geol. Sinica 77, 328–340 (in Chinese with English abstract).
Li, S.Z., Yang, Z.S., 1997. Types and genesis of Palaeoproterozoic granites in the Jiao-Liao Massif. Northwest Geol. 43, 21–27 (in Chinese with English abstract).
Li, S.Z., Zhao, G.C., Sun, M., Han, Z.Z., Zhao, G.T., Hao, D.F., 2006. Are the South and North Liaohe Groups of the North China Craton different exotic terranes? Nd isotope constraints. Gondwana Res. 9, 198–208.
Li, S.Z., Zhao, G.C., 2007. SHRIMP U–Pb zircon geochronology of the Liaoji granitoids: constraints on the evolution of the Paleoproterozoic Jiao-Liao-Ji belt in the eastern block of the North China craton. Precambrian Res. 158, 1–16.
Li, S.Z., Zhao, G.C., Santosh, M., Liu, X., Dai, L.M., 2011a. Palaeoproterozoic tectonothermal evolution and deep crustal processes in the Jiao-Liao-Ji Belt, North China Craton: a review. Geol. J. 46, 525–543.
Li, X.P., Guo, J.H., Zhao, G.C., Li, H.K., Song, Z.H., 2011b. Formation of the Paleoproterozoic calc-silicate and high-pressure mafic granulite in the Jiaobei terrane, eastern Shandong, China. Acta Petrol. Sinica 27, 961–968 (in Chinese with English abstract).
Li, Z., Chen, B., 2014. Geochronology and geochemistry of the Paleoproterozoic meta-basalts from the Jiao-Liao-Ji Belt, North China Craton: implications for petrogenesis and tectonic setting. Precambrian Res. 255, 653–667.
Litvinovsky, B.A., Jahn, B.M., Zanvilevich, A.N., Saunders, A., Poulain, S., Kuzmin, D.V., Reichow, M.K., Titov, A.V., 2002. Petrogenesis of syenite–granite suites from the Bryansky Complex (Transbaikalia, Russia): implications for the origin of A-type granitoid magmas. Chem. Geol. 189, 105–133.
Liu, D.Y., Nutman, A.P., Compston, W., Wu, J.S., Shen, Q.H., 1992. Remnants of ≥3800 Ma crust in the Chinese part of the Sino-Korean craton. Geology 20, 339–342.
Liu, J., Liu, F., Ding, Z., Liu, P., Guo, C., Wang, F., 2014. Geochronology, petrogenesis and tectonic implications of Paleoproterozoic granitoid rocks in the Jiaobei Terrane, North China Craton. Precambrian Res. 255, 685–698.
Liu, Y.S., Hu, Z.C., Gao, S., Günther, D., Xu, J., Gao, C.G., Chen, H.H., 2008. In situ analysis of Major and trace elements of anhydrous minerals by LA–ICP-MS without applying an internal standard. Chem. Geol. 257, 34–43.
Liu, Y.S., Hu, Z.C., Zong, K.Q., Gao, C.G., Gao, S., Xu, J., Chen, H.H., 2010. Reappraisement and refinement of zircon U–Pb isotope and trace element analyses by LA–ICP-MS. Chin. Sci. Bull. 55, 1535–1546.
Luo, Y., Sun, M., Zhao, G., Li, S., Xu, P., Ye, K., Xia, X., 2004. LA–ICP-MS U–Pb zircon ages of the Liaohe Group in the Eastern Block of the North China Craton: constraints on the evolution of the Jiao-Liao-Ji Belt. Precambrian Res. 134, 349–371.
Luo, Y., Sun, M., Zhao, G., Li, S., Ayers, J.C., Xia, X., Zhang, J., 2008. A comparison of U–Pb and Hf isotopic compositions of detrital zircons from the North and South Liaohe Groups: constraints on the evolution of the Jiao-Liao-Ji Belt, North China Craton. Precambrian Res. 163, 279–306.
Lu, L.Z., 1996. The Precambrian metamorphic geology and tectonic evolution of the Jiao-Liao massif. J. Changchun Univ. Earth Sci. 26, 25–32 (in Chinese with English abstract).
Lu, X.P., Wu, F.Y., Guo, J.H., Wilde, S.A., Yang, J.H., Liu, X.M., Zhang, X.O., 2006. Zircon U–Pb geochronological constraints on the Paleoproterozoic crustal evolution of the Eastern block in the North China Craton. Precambrian Res. 146, 138–164.
Lu, X.P., Wu, F.Y., Guo, J.H., Yin, C.J., 2005. Late Paleoproterozoic granitic magmatism and crustal evolution in the Tonghua region, northeast China. Acta Petrol. Sinica 21, 721–736 (in Chinese with English abstract).
Lu, X.P., Wu, F.Y., Lin, J.Q., Sun, D.Y., Zhang, Y.B., Guo, C.L., 2004. Geochronological successions of the early Precambrian granitic magmatism in southern Liaodong Peninsula and its constraints on tectonic evolution of the North China Craton. Chin. J. Geol. 39, 123–138 (in Chinese with English abstract).
Ludwig, K.R., 2003. User's Manual for Isoplot 3.00, a geolocronolgical Toolkit for Microsoft Excel. Berkeley Geochronlogical Center Special Publication 4, 25–32.
Lugmair, G.W., Harti, K., 1978. Lunar initial $^{143}Nd/^{144}Nd$: differential evolution of the lunar crust and mantle. Earth Planet. Sci. Lett. 39, 349–357.
Martin, R.F., 2006. A-type granites of crustal origin ultimately result from open-system fenitization-type reactions in an extensional environment. Lithos 91, 125–136.

Meng, E., Liu, F.L., Cui, Y., Cai, J., 2013. Zircon U–Pb and Lu–Hf isotopic and whole-rock geochemical constraints on the protolith and tectonic history of the Changhai metamorphic supracrustal sequence in the Jiao-Liao-Ji Belt, southeast Liaoning Province, northeast China. Precambrian Res. 233, 297–315.
Meng, E., Liu, F.L., Liu, P.H., Liu, C.H., Yang, H., Wang, F., Shi, J.R., Cai, J., 2014. Petrogenesis and tectonic significance of Paleoproterozoic meta-mafic rocks from central Liaodong Peninsula, northeast China: evidence from zircon U–Pb dating and in situ Lu–Hf isotopes, and whole-rock geochemistry. Precambrian Res. 247, 92–109.
Mushkin, A., Navon, O., Halicz, L., Hartmann, G., Stein, M., 2003. The petrogenesis of A-type magmas from the Amram Massif, Southern Israel. J. Petrol. 44, 815–832.
Nair, R., Chacko, T., 2002. Fluid-absent melting of high-grade semi-pelites: *P–T* constraints on orthopyroxene formation and implications for granulite genesis. J. Petrol. 43, 2121–2141.
Namur, O., Charlier, B., Toplis, M.J., Higgins, M.D., Hounsell, V., Liegeois, J., Auwera, J.V., 2011. Differentiation of tholeiitic basalt to A-type granite in the Sept Iles layered intrusion, Canada. J. Petrol. 52, 487–539.
Nesbitt, H.W., Young, G.M., 1982. Early Proterozoic climates and plate motions inferred from major element chemistry of lutites. Nature 299, 715–717.
Patiño Douce, A.E., 1997. Generation of metaluminous A-type granites by low-pressure melting of calc-alkaline granitoids. Geology 25, 743–746.
Patiño Douce, A.E., Beard, J.S., 1995. Dehydration-melting of biotite gneiss and quartz amphibolite from 3 to 15 kbar. J. Petrol. 36, 707–738.
Pearce, J.A., Harris, N.B.W., Tindle, A.G., 1984. Trace element discrimination diagrams for the tectonic interpretation of granitic rocks. J. Petrol. 25, 956–983.
Peng, P., Guo, J.H., Zhai, M.G., Windley, B.F., Li, T.S., Liu, F., 2012. Genesis of the Hengling magmatic belt in the North China Craton: implications for Paleoproterozoic tectonics. Lithos 148, 27–44.
Peng, Q.M., Palmer, M.R., 1995. The Palaeoproterozoic boron deposits in eastern Liaoning, China: a metamorphosed evaporite. Precambrian Res. 72, 185–197.
Peng, Q.M., Palmer, M.R., 2002. The Paleoproterozoic Mg and Mg–Fe borate deposits of Liaoning and Jilin Provinces, northeast China. Econ. Geol. 97, 93–108.
Pitcher, W.S., 1997. The Nature and Origin of Granite. Springer Science+Business Media, B.V, 387pp.
Sano, Y., Tsutsumi, Y., Terada, K., Kaneoka, I., 2002. Ion microprobe U–Pb dating of Quaternary zircon: implication for magma cooling and residence time. J. Volcanol. Geotherm. Res. 117, 285–296.
Santosh, M., 2010. Assembling North China Craton within the Columbia supercontinent: the role of double-sided subduction. Precambrian Res. 178, 149–167.
Singh, J., Johannes, W., 1996. Dehydration melting of tonalites. Part II. Composition of melts and solids. Contrib. Mineral. Petrol. 125, 26–44.
Skjerlie, K.P., Johnston, A.D., 1993. Fluid-absent melting behavior of an F-rich tonalitic gneiss at mid-crustal pressures: implications for the generation of anorogenic granites. J. Petrol. 34, 785–815.
Söderlund, U., Patchett, P.J., Vervoort, J.D., Isachsen, C.E., 2004. The ^{176}Lu decay constant determined by Lu–Hf and U–Pb isotope systematics of Precambrian mafic intrusions. Earth Planet. Sci. Lett. 219, 311–324.
Sun, M., Zhang, L.F., Wu, J.H., 1996. The origin of the Early Proterozoic Kuandian Complex: evidence from geochemistry. Acta Geol. Sinica 70, 207–222 (in Chinese with English abstract).
Sun, S.S., McDonough, W.F., 1989. Chemical and isotopic systematics of oceanic basalts: implications for mantle composition and processes. In: Saunders, A.D., Norry, M.J. (Eds.), Magmatism in the Oceanic Basalts. Geological Society Special Publication, pp. 313–345.
Tam, P.Y., Zhao, G., Sun, M., Li, S., Iizuka, Y., Ma, G.S.K., Yin, C., He, Y., Wu, M., 2012a. Metamorphic *P–T* path and tectonic implications of medium-pressure pelitic granulites from the Jiaobei massif in the Jiao-Liao-Ji Belt, North China Craton. Precambrian Res. 220–221, 177–191.
Tam, P.Y., Zhao, G., Sun, M., Li, S., Wu, M., Yin, C., 2012b. Petrology and metamorphic *P–T* path of high-pressure mafic granulites from the Jiaobei massif in the Jiao-Liao-Ji Belt, North China Craton. Lithos 155, 94–109.
Tam, P.Y., Zhao, G., Zhou, X., Sun, M., Guo, J., Li, S., Yin, C., Wu, M., He, Y., 2012c. Metamorphic *P–T* path and implications of high-pressure pelitic granulites from the Jiaobei massif in the Jiao-Liao-Ji Belt, North China Craton. Gondwana Res. 22, 104–117.
Tam, P.Y., Zhao, G.C., Liu, F.L., Zhou, X.W., Sun, M., Li, S.Z., 2011. Timing of metamorphism in the Paleoproterozoic Jiao-Liao-Ji Belt: new SHRIMP U–Pb zircon dating of granulites, gneisses and marbles of the Jiaobei Massif in the North China Craton. Gondwana Res. 19, 150–162.
Tang, J., Zheng, Y.F., Wu, Y.B., Song, B., Liu, X.M., 2007. Geochronology and geochemistry of metamorphic rocks in the Jiaobei terrane: constraints on its tectonic affinity in the Sulu orogen. Precambrian Res. 152, 48–82.
Tischendorf, G., Förster, H.J., Gottesmann, B., 2001. Minor- and trace-element composition of trioctahedral micas: a review. Mineral. Mag. 65, 249–276.
Turner, S.P., Foden, J.D., Morrison, R.S., 1992. Derivation of some A-type magmas by fractionation of basaltic magma: an example from the Padthaway Ridge, South Australia. Lithos 28, 151–179.
Uchida, E., Endo, S., Makino, M., 2007. Relationship between solidification depth of granitic rocks and formation of hydrothermal ore deposits. Resour. Geol. 57, 47–56.
Wan, Y.S., Song, B., Liu, D.Y., Wilde, S.A., Wu, J.S., Shi, Y.R., Yin, X.Y., Zhou, H.Y., 2006. SHRIMP U–Pb zircon geochronology of Paleoproterozoic metasedimentary rocks in the North China Craton: evidence for a major Late Paleoproterozoic tectonothermal event. Precambrian Res. 149, 249–271.
Wang, F., Liu, F.L., Liu, P.H., Liu, J.H., 2010. Metamorphic evolution of Early Precambrian khondalite series in North Shandong Province. Acta Petrol. Sinica 26, 2057–2072 (in Chinese with English abstract).
Wang, S.T., Gao, M.X., Wan, Z.J., Sun, S.L., 2007. Geological characteristics of Paleoproterozoic metamorphic sedimentary iron deposit in east part of Changyi area in Shandong Province. Shandong Land Resour. 23, 45–48 (in Chinese with English abstract).
Watson, E.B., Harrison, T.M., 1983. Zircon saturation revisited: temperature and composition effects in a variety of crustal magma types. Earth Planet. Sci. Lett. 64, 295–304.
Whalen, J.B., Currie, K.L., Chappell, B.W., 1987. A-type granites: geochemical characteristics, discrimination and petrogenesis. Contrib. Mineral. Petrol. 95, 407–419.
White, A.J.R., 1979. Sources of Granitic Magma. Abstracts of Papers to be Presented at the Annual Meetings of the Geological Society of America and Associated Societies, San Diego, CA, vol. 11., pp. 539.
White, A.J.R., Chappell, B.W., 1983. Granitoid types and their distribution in the Lachlan Fold Belt, southeastern Australia. Geol. Soc. Am. Mem. 159, 21–34.
Woodhead, J., Hergt, J., 2005. A preliminary appraisal of seven natural zircon reference materials for in situ Hf isotope determination. Geostand. Geoanal. Res. 29, 183–195.
Wright, J.B., 1969. A simple alkalinity ratio and its application to questions of non-orogenic granite genesis. Geol. Mag. 106, 370–384.
Wu, F.Y., Sun, D.Y., Li, H., Jahn, B.M., Wilde, S.A., 2002. A-type granites in Northeastern China: age and geochemical constraints on their petrogenesis. Chem. Geol. 187, 143–173.
Wu, Y., Zheng, Y., 2004. Genesis of zircon and its constraints on interpretation of U–Pb age. Chin. Sci. Bull. 49, 1554–1569.
Xie, L.W., Zhang, Y.B., Sun, J.F., Wu, F.Y., 2008. In situ simultaneous determination of trace elements, U–Pb and Lu–Hf isotopes in zircon and baddeleyite. Chin. Sci. Bull. 53, 1565–1573.
Xu, W.L., Zhou, Q.J., Pei, F.P., Yang, D.B., Gao, S., Li, Q.L., Yang, Y.H., 2013. Destruction of the North China Craton: delamination or thermal/chemical erosion? Mineral chemistry and oxygen isotope insights from websterite xenoliths. Gondwana Res. 23, 119–129.
Xu, Y.G., Li, H.Y., Pang, C.J., He, B., 2009. On the timing and duration of the destruction of the North China Craton. Chin. Sci. Bull. 54, 3379–3396.
Yang, C.H., Du, L.L., Ren, L.D., Song, H.X., Wan, Y.S., Xie, H.Q., Liu, Z.X., 2011. The age and petrogenesis of the Xuting granite in the Zanhuang Complex, Hebei Province: constraints on the structural evolution of the Trans-North China Orogen, North China Craton. Acta Petrol. Sinica 27, 1003–1016 (in Chinese with English abstract).
Yang, D.B., Xu, W.L., Pei, F.P., Wang, Q.H., 2009. Petrogenesis of the Paleoproterozoic K-feldspar granites in Bengbu Uplift: constraints from petro-geochemistry, zircon U–Pb dating and Hf isotope. Earth Sci. J. China Univ. Geosci. 34, 148–164.
Yang, J.H., Wu, F.Y., Chung, S.L., Wilde, S.A., Chu, M.F., 2006. A hybrid origin for the Qianshan A-type granites, northeast China: geochemical and Sr–Nd–Hf isotopic evidence. Lithos 89, 89–106.
Yu, Z.C., 1996. New progress of research on the Fenzishan Group in the Pingdu-Laizhou area in the west of Jiaobei region. Shandong Geol. 12, 24–34 (in Chinese with English abstract).
Yuan, H.L., Gao, S., Dai, M.N., Zong, C.L., Günther, D., Fontaine, G.H., Liu, X.M., Diwu, C.R., 2008. Simultaneous determinations of U–Pb age, Hf isotopes and trace element compositions of zircon by excimer laser-ablation quadrupole and multiple-collector ICP-MS. Chem. Geol. 247, 100–118.
Zhai, M.G., Santosh, M., 2011. The Early Precambrian odyssey of the North China Craton: a synoptic overview. Gondwana Res. 20, 6–25.
Zhang, H.F., Zhu, R.X., Santosh, M., Ying, J.F., Su, B.X., Hu, Y., 2013. Episodic widespread magma underplating beneath the North China Craton in the Phanerozoic: implications for craton destruction. Gondwana Res. 23, 95–107.
Zhang, Q.S., Yang, Z.S., 1988. Early Crust and Mineral Deposits of Liaodong Peninsula, China. Geological Publishing House, Beijing, pp. 218–450 (in Chinese with English abstract).
Zhao, G.C., 2001. Paleoproterozoic assembly of the North China Craton. Geol. Mag. 138, 87–91.
Zhao, G.C., Cawood, P.A., 2012. Precambrian geology of China. Precambrian Res. 222–223, 13–54.
Zhao, G., Cawood, P.A., Li, S., Wilde, S.A., Sun, M., Zhang, J., He, Y., Yin, C., 2012. Amalgamation of the North China Craton: key issues and discussion. Precambrian Res. 222–223, 55–76.
Zhao, G.C., Sun, M., Wilde, S.A., Li, S.Z., 2005. Late Archean to Paleoproterozoic evolution of the North China Craton: key issues revisited. Precambrian Res. 136, 177–202.
Zhao, G.C., Wilde, S.A., Cawood, P.A., Sun, M., 2001. Archean blocks and their boundaries in the North China Craton: lithological, geochemical, structural and *P–T* path constraints and tectonic evolution. Precambrian Res. 107, 45–73.
Zhao, G.C., Wilde, S.A., Sun, M., Li, S.Z., Li, X.P., Zhang, J., 2008. SHRIMP U–Pb zircon ages of granitoid rocks in the Lüliang Complex: implications for the accretion and evolution of the Trans-North China Craton Orogen. Precambrian Res. 160, 213–226.
Zhao, G., Zhai, M., 2013. Lithotectonic elements of Precambrian basement in the North China Craton: review and tectonic implications. Gondwana Res. 23, 1207–1240.

Zhou, X.W., Wei, C.J., Geng, Y.S., 2007. Phase equilibria and P-T path of high- and low-pressure pelitic granulites from the Jiaobei massif. Earth Sci. Front. 14, 135–143 (in Chinese with English abstract).
Zhou, X.W., Zhao, G.C., Wei, C.J., Geng, Y.S., Sun, M., 2008. EPMA U–Th–Pb monazite and SHRIMP U–Pb zircon geochronology of high-pressure pelitic granulites in the Jiaobei Massif of the North China Craton. Am. J. Sci. 308, 328–350.
Zhou, Y., Zhai, M., Zhao, T., Lan, Z., Sun, Q., 2014. Geochronological and geochemical constraints on the petrogenesis of the early Paleoproterozoic potassic granite in the Lushan area, southern margin of the North China Craton. J. Asian Earth Sci. 94, 190–204.
Zhu, R.X., Xu, Y.G., Zhu, G., Zhang, H.F., Xia, Q.K., Zheng, T.Y., 2012. Destruction of the North China Craton. Sci. China Earth Sci. 55, 1565–1587.
Zindler, A., Hart, S., 1986. Chemical geodynamics. Annu. Rev. Earth Planet. Sci. 14, 493–571.